International Journal of Multiphase Flow 142 (2021) 103718

Contents lists available at ScienceDirect

International Journal of Multiphase Flow

journal homepage: www.elsevier.com/locate/ijmulflow

Numerical simulation of a normally incident shock wave – dense particles layer interaction using the Godunov solver for the Baer–Nunziato equations

Ya.E. Poroshyna[a,b], P.S. Utkin[a,b,*]

[a] Institute for Computer Aided Design of the Russian Academy of Sciences, Moscow, Russia
[b] Moscow Institute of Physics and Technology, Dolgoprudny, Russia

ARTICLE INFO

Article history:
Received 3 September 2020
Revised 11 January 2021
Accepted 1 June 2021
Available online 6 June 2021

Keywords:
Numerical simulation
Shock wave
Intergranular stresses
Compaction wave
Particles layer
Baer-Nunziato equations
Godunov method
Pressure relaxation

ABSTRACT

The work is devoted to the numerical simulation of the known problem of a normally incident shock wave – dense layer of particles interaction and the phenomenon of the pressure rise on the wall under the layer. The novelty of the work is in the numerical approach which is based on the Godunov solver for the Baer-Nunziato equations and the pressure relaxation procedure which takes into account intergranular stresses in the solid phase. The algorithm based on the exact solution of the Riemann problem provides a low numerical dissipation of the solid contacts and is robust at the explicit interfacial boundaries. The algorithm was described in detail; the source code of the Godunov solver for the Baer-Nunziato equations was provided. The full scale experiment of a shock wave – particles layer interaction was simulated. The shape of the pressure curve, obtained on the wall under the particles layer, was explained from the point of view of ongoing wave processes in the layer. A quantitative comparison of the experimental and simulated pressure curves was carried out. Studies of the influence of parameters in the intergranular stresses model on simulation results as well as reversible or irreversible character of loading-unloading process were conducted. Obtained results were compared to the published simulation results by the other authors based on the R.I. Nigmatulin models.

1. Introduction

Interaction of an air shock wave (SW) with an interface boundary of two-phase gas-particles medium has been extensively studied over the last several decades. One of the major focuses of this study has been the attenuation of SWs by granular filters. A range of experimental and numerical works has been carried out studying propagation of a SW in a channel and its interaction with a granular or porous material located near the end wall of the channel. It was experimentally indicated in (Gelfand et al., 1975) that the peak pressure registered by a transducer on the wall behind polyurethane foam was significantly higher than pressure detected under the normal reflection of a SW of the same Mach number from the rigid wall. Although the experimental research in (Skews, 1991) was primarily focused on the dynamics of waves reflected from the interfacial boundary back into the gas, the gradual increase of the back wall pressure was also indicated. In (Baer, 1992), the Baer-Nunziato (BN) model (Baer and Nunziato, 1986) was applied in attempt to describe this complicated physical process numerically and simulate the experiments (Skews, 1991). It was stated that after the shock hit the foam a compaction wave (CW) occurred in the foam as gas permeated into the porous material imparting momentum to the solid phase. Later this phenomenon was investigated in a number of experimental (Skews et al., 1993), (Ben-Dor et al., 1994), (Yasuhara et al., 1996), (Seitz and Skews, 2006) and theoretical (Olim et al., 1994), (Mazor et al., 1994) studies.

Our interest was in the development of approaches to numerical simulation of the interaction of a SW with a layer of particles on an impenetrable surface using the BN model. Apparently, after (Baer, 1992) the most significant progress in this field took place in (Saurel and Abgrall, 1999) and numerous subsequent works of these authors, see a review in (Utkin, 2019). The key advantage of the BN model and its possible extensions in comparison with other two-phase models is the hyperbolicity of the BN equations. Although the defining system of equations is hyperbolic, it can not be written in the conservative form due to the so-called nozzling

* Corresponding author.
E-mail address: pavel_utk@mail.ru (P.S. Utkin).

https://doi.org/10.1016/j.ijmultiphaseflow.2021.103718

terms in the right hand side of the system that are associated with the local gradient of the volume fraction of the solid phase. A correct approximation of these terms is one of the difficulties that arise while solving the BN system of equations. However, the hyperbolicity of the BN equations has led to an extensive work on the development of the numerical schemes for its solution. The HLL (Saurel and Abgrall, 1999), HLLC (Tokareva and Toro, 2010), (Furfaro, Saurel, 2015), (Lochon et al., 2016), (Hennessey et al., 2020), HLLEM (Dumbser, Balsara, 2016), AUSM (Tokareva, Toro, 2016), Godunov (Schwendeman et al., 2006), Rusanov (Saurel and Abgrall, 1999), (Menshov, Serezhkin, 2018) and a number of other schemes for the solution of the BN equations were developed. Meanwhile, the efficiency of many of the proposed schemes was shown only on the academic test cases like the Riemann problem. Usage of these schemes for solution of practical problems is often a challenging issue due to the special cases as the vanishing phase case, see the terminology in (Schwendeman et al., 2006), when the solid phase vanishes in some regions of the computational domain. For example, the original HLLC method (Tokareva and Toro, 2010) did not address the vanishing phase case and it was improved later in (Lochon et al., 2016) and applied for the simulation of a shock-bubble interaction and an underwater explosion. The Godunov method (Schwendeman et al., 2006) is in the similar status. Although the vanishing phase case was described in (Schwendeman et al., 2006), a robust numerical algorithm of the Godunov method for all solid phase volume fraction cases was not presented. As well as its application to the real life problems with the exception of the simulations of deflagration and detonation waves initiation and propagation in the heterogeneous explosives (Schwendeman et al., 2008). At the same time, the Godunov method is a physically relevant approach for solution of the BN equations with the minimal number of additional assumptions or simplifications. In (Fraysse et al., 2016) the comparison of different numerical methods for solution of the BN equations was carried out on a set of test Riemann problems. The Godunov (Schwendeman et al., 2006) and the HLLC (Tokareva and Toro, 2010) methods were noticed as the most accurate for all considered test cases. However, test cases in (Fraysse et al., 2016) also did not contain problems with the vanishing solid phase. Computational cost of the Godunov method was considered to be one of the major disadvantages. But in contrast to the HLLC method for the Euler equations, the HLLC method for the BN equations (Tokareva and Toro, 2010) also demands the iterative solution of the system of non-linear algebraic equations. The Godunov method is of our interest in this work due to its distinctive properties among all Riemann solvers.

Previously we considered the problem of interaction of a SW with a moving cloud of particles with free boundaries in (Utkin, 2017), (Utkin, 2019). The initial volume fraction of particles corresponded to the dense column in the experiments (Rogue et al., 1998). It was possible to reproduce the features of the reflected and transmitted waves and the dynamics of the cloud movement correctly without intergranular stresses in the solid phase taken into account due to the free boundaries of the cloud and its fast dispersion. Nevertheless, this factor was taken into consideration in (Saurel et al., 2017). Intergranular stresses are important in the problems with the underlying surface when a traveling SW interacts with a dust layer, see (Fan et al., 2007), for instance. The first and the main goal of this work was the development of the numerical algorithm for the solution of the BN system of equations using the Godunov method (Schwendeman et al., 2006) taking into account intergranular stresses in the pressure relaxation procedure. The algorithm has to be robust for the simulations with explicit interfacial boundaries.

Moreover, we intended to examine the problem of interaction of a SW with a particles bed located near the rigid wall described in (Gelfand et al., 1989). In the recent study (Sugiyama et al., 2021), a similar mathematical model (BN-type equations and intergranular stresses model from (Saurel et al., 2010)) was used for the three-dimensional simulations of a blast wave interaction with a layer of glass particles. The HLLC (Furfaro, Saurel, 2015) numerical method was used. Apparently, the approach of (Furfaro, Saurel, 2015) is more computationally efficient than (Tokareva and Toro, 2010) and the subsequent developments (Lochon et al., 2016), (Hennessey et al., 2020), although this issue was not analyzed, for example, in (Fraysse et al., 2016). However, the HLLC method (Furfaro, Saurel, 2015) is also not so widespread in two-phase simulations. One of the possible reasons is that the HLLC method (Furfaro, Saurel, 2015) is formulated in the ideology of discrete element method (Abgrall, Saurel, 2003) that differs from the general finite volume method notations.

In (Britan et al., 1997), the process of SW – dense particles layer interaction was studied experimentally and numerically. It was indicated that the pressure curve near the back wall consisted of the initial oscillations connected with the CW propagation and the subsequent steady rise of the pressure during gas filtration. Experiments (Britan et al., 1995) later simulated in (Surov, 2000) demonstrated that oscillatory behavior is not inherent in gas-liquid foams in contrast to porous medium. If the particles layer length was small, the pressure rise on the wall was provided by the action of the CW. The longer the particles layer was, the less was the value of the peak pressure. A terminology comment should be made. Compaction is an irreversible process which leads to the hysteresis phenomenon when the granular media is subjected to a loading – unloading cycle (Saurel et al., 2010). However, if the loads are not very strong in comparison with the plastic limit of the granular material, intergranular stresses lead to the reversible process of powder loading – unloading process. A wave in which both volume fraction and density of the solid phase are changed will be referred to as CW in any case.

It was also stated in (Kutushev and Rodionov, 1999) and (Gubaidullin et al., 2003) that a filtration wave in gas and a deformation wave in the solid phase could be observed due to a SW – bed of particles interaction. A deformation wave in the skeleton of a porous medium occurred under the influence of such forces as the "Archimedes" force $\bar{\alpha} \cdot \partial p / \partial x$, where $\bar{\alpha}$ is the solid phase volume fraction and p is the gas phase pressure, interfacial friction, the gradient of intergranular stress of the solid phase and particles inertia. However, the Archimedes force was stated to contribute the most to the formation of pressure pulses on the back wall.

In (Britan and Ben-Dor, 2006), different particles were considered and it was experimentally shown that there was an optimal particles layer length that led to the maximum value of the peak pressure on the back wall. This layer length was different for the particles with various sizes and densities. It was stated that, in contrast to the high-porosity foams, interaction of waves was not so important within the granular samples for the formation of the pressure peaks on the back wall. As generally the porosity is far lower in the granular materials than in foams, the waves attenuate quickly in the sample, so the waves' interaction contributes most to the pressure peaks formation in the rather short granular beds. Otherwise, it is the gas filtration that plays the major role in the increase of pressure on the back wall as well as such effects as the dry friction, rotation of particles and reduction of the porous space. However, provided the incident SW is rather strong, it is the compaction that makes the greatest contribution to the pressure increase. It explains why numerical models that do not account for the gas filtration are still able to describe the experimental results for the strong SWs with the good agreement (see, for instance, the application of the BN model in (Baer, 1988)). So, the second goal of this work is the numerical study of the qualitative and quantitative characteristics of the SW – particles layer interaction (Gelfand et al., 1989) (the phenomenon of the pressure rise on the wall under the layer, the amplitude of the main pressure peak, the oscillatory nature of the pressure curve) using the BN model in comparison with the simulations from (Kutushev and Rudakov, 1993) in which the R.I. Nigmatulin model (Nigmatulin, 1990) was used.

This paper is organized as follows. Section 2 outlines the defining system of equations. In Section 3, the numerical algorithm used in this study is presented in detail. Attention is paid both to the hyperbolic step of the algorithm (Section 3.1) also clarified in the Appendix and to the pressure relaxation step taking into account intergranular stresses (Section 3.2). In Section 4. two verification problems are considered. Section 4.1 addresses the Riemann problem for the reduced BN system of equations. In Section 4.2. the problem of SW – particles cloud interaction (Rogue et al., 1998) is examined. Section 5 covers simulations of the experiment (Gelfand et al., 1989) on a SW – particles layer on the wall interaction including both reversible (Section 5.2) and irreversible (Section 5.3) models. In Section 6. we discuss obtained results in the scope of existing simulations of SW – particles layer interaction problem. The conclusions are drawn in the final Section.

2. Mathematical model

The mathematical model was based on the BN system of equations (Baer and Nunziato, 1986) with modifications and improvements from (Bdzil et al., 1999), (Saurel and Abgrall, 1999) and (Saurel et al., 2010):

$$\mathbf{u}_t + \mathbf{f}_x(\mathbf{u}) = \mathbf{h}(\mathbf{u})\bar{\alpha}_x + \mathbf{p} + \mathbf{s}, \tag{1}$$

$$\mathbf{u} = \begin{bmatrix} \bar{\alpha} \\ \bar{\alpha}\bar{\rho} \\ \bar{\alpha}\bar{\rho}\bar{v} \\ \bar{\alpha}\bar{\rho}\bar{E} \\ \alpha\rho \\ \alpha\rho v \\ \alpha\rho E \end{bmatrix}, \mathbf{f} = \begin{bmatrix} 0 \\ \bar{\alpha}\bar{\rho}\bar{v} \\ \bar{\alpha}(\bar{\rho}\bar{v}^2+\bar{p}) \\ \bar{\alpha}\bar{v}(\bar{\rho}\bar{E}+\bar{p}) \\ \alpha\rho v \\ \alpha(\rho v^2+p) \\ \alpha v(\rho E+p) \end{bmatrix}, \mathbf{h} = \begin{bmatrix} -\tilde{v} \\ 0 \\ \tilde{p} \\ \tilde{p}\tilde{v} \\ 0 \\ -\tilde{p} \\ -\tilde{p}\tilde{v} \end{bmatrix}, \mathbf{p} = \begin{bmatrix} F \\ 0 \\ 0 \\ -(\tilde{p}+\beta)F \\ 0 \\ 0 \\ \tilde{p}F \end{bmatrix},$$

$$\mathbf{s} = \begin{bmatrix} 0 \\ 0 \\ -f \\ -f\cdot\tilde{v} \\ 0 \\ f \\ f\cdot\tilde{v} \end{bmatrix},$$

$$\bar{\alpha} + \alpha = 1,$$

$$\bar{E} = \frac{\bar{v}^2}{2} + \bar{e}(\bar{p},\bar{\rho}) = \frac{\bar{v}^2}{2} + \frac{\bar{p}+\bar{\gamma}\bar{\pi}_0}{\bar{\rho}(\bar{\gamma}-1)}, E = \frac{v^2}{2} + e(p,\rho) = \frac{v^2}{2} + \frac{p+\gamma\pi_0}{\rho(\gamma-1)},$$

$$F = \frac{\alpha\bar{\alpha}}{\mu_c}(\bar{p} - p - \beta).$$

Here t is the time, x is the space coordinate, α is the volume fraction, ρ is the true density, v is the velocity, p is the pressure, E is the specific total energy, e is the specific internal energy, $\bar{\gamma}$ and $\bar{\pi}_0$ are the parameters in the stiffened gas equation of state (EOS) for the solid phase of particles, γ and π_0 are the analogues parameters for the gas phase EOS, μ_c is the coefficient of compaction viscosity, β is the configuration pressure or intergranular stress. The bar superscript was used to indicate solid phase quantities. In simulations, the ideal gas EOS for the gas phase was used with $\pi_0 = 0$. However, we left this parameter in the formulas of the numerical algorithm further so that it is valid for other problems. For example, stiffened gas EOS for both phases is necessary for the simulation of high-speed impact of two metal plates using two-fluid approach (Utkin and Fortova, 2018).

Nozzling term $\mathbf{h}(\mathbf{u})\bar{\alpha}_x$ is the specific feature of the BN system of equations. Velocity $\tilde{v}$ and pressure $\tilde{p}$ are interfacial variables. They were chosen as in (Baer and Nunziato, 1986), although other options were also possible (Saurel et al., 2010), (Lallemand et al., 2005):

$$\tilde{p} = p, \tilde{v} = \bar{v}.$$

Vector $\mathbf{p}$ contains pressure relaxation terms. Following (Saurel et al., 2010), two approaches for the pressure relaxation were considered. The first one corresponds to the stiff local interfacial boundary equilibrium and, consequently, the reversible loading-unloading of the particles layer. The second approach implies a switch between a stiff relaxation and a compaction with a finite rate F and refers to the irreversible compaction. For a stiff relaxation the following mechanical equilibrium condition at the interfacial boundary is used (Baer and Nunziato, 1986), (Saurel et al., 2010):

$$\bar{p} = \tilde{p} + \beta, \tag{2}$$

$$\beta = \bar{\alpha}\bar{\rho}\frac{dB}{d\bar{\alpha}} = -\bar{\alpha}\bar{\rho}\cdot a\cdot n\cdot\ln\frac{1-\bar{\alpha}}{1-\bar{\alpha}_0}\left(\frac{B(\bar{\alpha})}{a}\right)^{\frac{n-1}{n}}, \tag{3}$$

$$B(\overline{\alpha}) = \begin{cases} B_a(\overline{\alpha}), & \text{if } \overline{\alpha}_{\text{crit}} < \overline{\alpha} < 1, \\ 0, & \text{otherwise}, \end{cases} \tag{4}$$

$$B_a(\bar{\alpha}) = a[b_1(\bar{\alpha}) - b_1(\bar{\alpha}_{\text{crit}}) + b_2(\bar{\alpha})]^n, \tag{5}$$

$$b_1(\bar{\alpha}) = (1-\bar{\alpha})\ln(1-\bar{\alpha}), b_2(\bar{\alpha}) = (1+\ln(1-\bar{\alpha}_{\text{crit}}))(\bar{\alpha}-\bar{\alpha}_{\text{crit}}). \tag{6}$$

Here $B(\bar{\alpha})$ is the potential energy of compaction, a and n are the empirical coefficients that characterize a considered two-phase medium , $\bar{\alpha}_{\text{crit}}$ is a threshold value of the solid phase volume fraction. If $\bar{\alpha}$ exceeds $\bar{\alpha}_{\text{crit}}$, compaction is enabled and $B(\bar{\alpha})$ becomes greater than 0. The model (2) – (6) was developed in (Saurel et al., 2010) after simulation of reversible and irreversible powders compaction on the basis of a two-phase one-velocity BN-type approach. The values of $\bar{\alpha}_{\text{crit}}$, a and n were obtained from the analysis of the experimental data on quasi-static compression of different powders. The relations, resembling (4) and (5), might be found in older works devoted to the internal ballistics problems (Koo et al., 1976). In those works intergranular stress was used as pressure in solid phase of gun powder granules that prevented their excessive compaction during the shot. In (Favrie and Gavrilyuk, 2013) the model (Saurel et al., 2010) was improved in order to take into account elastic and plastic deformations simultaneously. The model (Saurel et al., 2010) was extended to the two-velocity model later in (Saurel et al., 2014) and to the model for dilute and dense two-phase flows (Saurel et al., 2017). The relations (3)– (6) were also used in the work (McGrath et al., 2016). However, the details of the numerical algorithm including the treatment of vanishing solid phase case were omitted in (McGrath et al., 2016).

Vector $\mathbf{s}$ in (2) took into account source terms. The drag force f was defined following (Gidaspow, 1994), (Houim and Oran, 2016):

$$f = K(\bar{v} - v),$$

$$K = \begin{cases} 0.75C_d\frac{\rho\alpha\bar{\alpha}|\bar{v}-v|}{d\alpha^{2.65}}, \text{ if}\alpha \geq 0.8, \\ \frac{150\bar{\alpha}^2\mu_{\text{vis}}}{\alpha d^2} + 1.75\frac{\rho\bar{\alpha}|\bar{v}-v|}{d}, \text{ if}\alpha < 0.8, \end{cases}$$

$$C_d = \begin{cases} \frac{24}{\alpha\text{Re}}\left[1+0.15(\alpha\text{Re})^{0.687}\right], \text{ if}\alpha\text{Re} < 10^3, \\ 0.44, \text{ if}\alpha\text{Re} \geq 10^3, \end{cases}$$

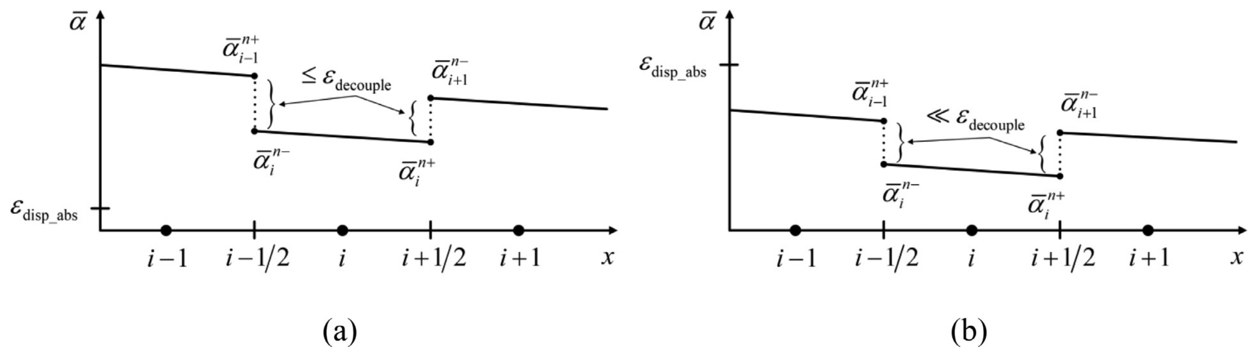

Fig. 1. The schematic of phases complete decoupling case: (a) a solid phase exists in cells i, $i \pm 1$, (b) a solid phase is absent in cells i, $i \pm 1$.

$$\mathrm{Re} = \frac{\rho|\bar{v} - v|d}{\mu_{\text{vis}}},$$

where d is the particles' diameter, μ_{vis} is the dynamic gas viscosity coefficient.

3. Numerical algorithm

The computational algorithm was based on the Strang splitting principle:

$$\mathbf{U}_j^{n+1} = L_s L_{\text{relax}} L_{\text{h}} \mathbf{U}_j^n. \tag{7}$$

Here $\mathbf{U}_j^{n+1}$ is the unknown grid function, j is the spatial index, n is the time index. At the hyperbolic stage of the algorithm denoted as operator L_{h}, the defining system of equations (1) was solved with $\mathbf{p} = \mathbf{0}$ and $s = 0$. After that a pressure relaxation procedure L_{relax} was implemented. Finally, non-differential algebraic source terms that describe interfacial interaction were taken into account and this step of the algorithm was denoted as L_s.

3.1. Hyperbolic step

The computational domain was a one-dimensional segment of the length L which is divided into N uniform cells. The cells were enumerated using index i from 1 to N. The size of the computational cell was $\Delta x = L/N$. The construction of a finite-volume scheme for the current computational cell i started with the analysis of the gaps $|\bar{\alpha}_{i-1}^{n+} - \bar{\alpha}_i^{n-}|$ and $|\bar{\alpha}_{i+1}^{n-} - \bar{\alpha}_i^{n+}|$ (see Fig. 1). Signs "+" and "–" in the superscripts in Fig. 1 denote the reconstructed values. For the increase of the accuracy order in space, a component-wise reconstruction of the conservative vectors in the computational cells using a minmod limiter was carried out:

$$\mathbf{U}_i^{n\pm} = \mathbf{U}_i^n \pm \frac{1}{2}\Delta x (\partial \mathbf{U}/\partial x)_i^n,$$

$$(\partial \mathbf{U}/\partial x)_i^n = \operatorname{minmod}\left(\frac{\mathbf{U}_i^n - \mathbf{U}_{i-1}^n}{\Delta x}, \frac{\mathbf{U}_{i+1}^n - \mathbf{U}_i^n}{\Delta x}\right), i = 2, ..., N-1, \tag{8}$$

$$\psi(a, b) = \frac{1}{2}(\operatorname{sign}(a) + \operatorname{sign}(b)) \cdot \min(|a|, |b|).$$

Formula (8) was valid for the inner cells of the computational domain. For the boundary cells, the gradients of the conservative vector components were taken equal to zero:

$$\left(\frac{\partial \mathbf{U}}{\partial x}\right)_1^n = \left(\frac{\partial \mathbf{U}}{\partial x}\right)_N^n = 0.$$

We will now consider possible situations for the relation between $\bar{\alpha}_{i-1}^{n+}$ and $\bar{\alpha}_i^{n-}$, $\bar{\alpha}_i^{n+}$ and $\bar{\alpha}_{i+1}^{n-}$.

3.1.1. Case of phases complete decoupling

This case was characterized by the following relations:

$$\left|\bar{\alpha}_{i-1}^{n+} - \bar{\alpha}_i^{n-}\right| \leq \varepsilon_{\text{decouple}}, \left|\bar{\alpha}_{i+1}^{n-} - \bar{\alpha}_i^{n+}\right| \leq \varepsilon_{\text{decouple}}, \tag{9}$$

where $\varepsilon_{\text{decouple}}$ was a small positive number. This case included both situations when a solid phase was present or absent in neighbor cells. A solid phase was considered to be absent in a cell when $\bar{\alpha}$ was less than $\varepsilon_{\text{disp\_abs}}$, where $\varepsilon_{\text{disp\_abs}}$ was also a small positive number. The relation $\varepsilon_{\text{decouple}} \gg \varepsilon_{\text{disp\_abs}}$ was considered to be true. In the present work, the following small constants were used in all simulations: $\varepsilon_{\text{decouple}} = 10^{-3}$, $\varepsilon_{\text{disp\_abs}} = 10^{-6}$.

Both inequalities (9) should be valid simultaneously. The gradient $\bar{\alpha}_x$ was considered to be zero in cells i, $i \pm 1$ and the defining system (1) was split into two independent subsystems of Euler-type equations for each phase:

$$\widehat{\mathbf{u}}_t^{dec} + \widehat{\mathbf{f}}_x^{dec}\left(\widehat{\mathbf{u}}^{dec}\right) = 0,\ \widehat{\mathbf{u}}^{dec} = \begin{bmatrix} \overline{\alpha\rho} \\ \overline{\alpha\rho v} \\ \overline{\alpha\rho E} \end{bmatrix} = \bar{\alpha}\cdot \widehat{\mathbf{u}},\ \widehat{\mathbf{f}}^{dec} = \begin{bmatrix} \overline{\alpha\rho v} \\ \bar{\alpha}\left(\overline{\rho v^2} + \bar{p}\right) \\ \bar{\alpha}\left(\overline{\rho E} + \bar{p}\right) \end{bmatrix} = \bar{\alpha}\cdot \widehat{\mathbf{f}}, \tag{10}$$

$$\widehat{\mathbf{u}}_t^{dec} + \widehat{\mathbf{f}}_x^{dec}\left(\widehat{\mathbf{u}}^{dec}\right) = 0,\ \widehat{\mathbf{u}}^{dec} = \begin{bmatrix} \alpha\rho \\ \alpha\rho v \\ \alpha\rho E \end{bmatrix} = \alpha\cdot \widehat{\mathbf{u}},\ \widehat{\mathbf{f}}^{dec} = \begin{bmatrix} \alpha\rho v \\ \alpha\left(\rho v^2 + p\right) \\ \alpha(\rho E + p) \end{bmatrix} = \alpha\cdot \widehat{\mathbf{f}}. \tag{11}$$

Since $\bar{\alpha}_x = 0$, then $\bar{\alpha} = \text{const}$ and $\alpha = \text{const}$. So, each of the systems (10) and (11) was solved using the classical Godunov method for the single phase Euler equations (Godunov et al., 1976) according to the realization details in (Toro, 2009):

$$\frac{\widehat{\mathbf{U}}_i^{n+1} - \widehat{\mathbf{U}}_i^n}{\Delta t^n} + \frac{\widehat{\mathbf{F}}_{i+1/2}^{\text{Godunov}}\left(\widehat{\mathbf{U}}_i^{n+}, \widehat{\mathbf{U}}_{i+1}^{n-}\right) - \widehat{\mathbf{F}}_{i-1/2}^{\text{Godunov}}\left(\widehat{\mathbf{U}}_{i-1}^{n+}, \widehat{\mathbf{U}}_i^{n-}\right)}{\Delta x} = 0,$$

$$\frac{\widehat{\mathbf{U}}_i^{n+1} - \widehat{\mathbf{U}}_i^n}{\Delta t^n} + \frac{\widehat{\mathbf{F}}_{i+1/2}^{\text{Godunov}}\left(\widehat{\mathbf{U}}_i^{n+}, \widehat{\mathbf{U}}_{i+1}^{n-}\right) - \widehat{\mathbf{F}}_{i-1/2}^{\text{Godunov}}\left(\widehat{\mathbf{U}}_{i-1}^{n+}, \widehat{\mathbf{U}}_i^{n-}\right)}{\Delta x} = 0.$$

A time-step Δt^n was chosen dynamically from the stability condition:

$$\Delta t^n = \text{CFL} \cdot \min_i\left(\frac{\Delta x}{\left|v_i^n\right| + c_i^n}, \frac{\Delta x}{\left|\bar{v}_i^n\right| + \bar{c}_i^n}\right),$$

$$c = \sqrt{\gamma\frac{p + \pi_0}{\rho}},\ \bar{c} = \sqrt{\bar{\gamma}\frac{\bar{p} + \bar{\pi}_0}{\bar{\rho}}}, \tag{12}$$

where c is the speed of sound, CFL is the coefficient ranging from 0 to 1.

The case of phases complete decoupling was the most trivial one among the considered. At the same time, it was most often implemented in the simulations because it corresponded to the subdomains with pure gas and subdomains inside the particles layer at some distance from it boundaries. A solid phase volume fraction remained unchanged in the cell i and was updated on the next time step: $\bar{\alpha}_i^{n+1} = \bar{\alpha}_i^n$. Therefore, in case of phases complete decoupling, vector of conservative variables at the end of the hyperbolic step was as follows:

$$\mathbf{U}_i^{n+1} = \begin{bmatrix} \overline{\alpha}_i^n \\ \overline{\alpha}_i^n \widehat{\mathbf{U}}_i^{n+1} \\ \alpha_i^n \widehat{\mathbf{U}}_i^{n+1} \end{bmatrix}.$$

3.1.2. Case of a solid phase volume fraction gap

Suppose now that at least one of the conditions (9) (for instance, the second one for the edge $i+1/2$) was not valid. Then the decoupling approach from the Section 3.1.1 was applied for another edge only and provided not the updated conservative variables vector in the current cell i but only the numerical flux vector:

$$\mathbf{F}_R\left(\mathbf{U}_{i-1}^{n+}, \mathbf{U}_i^{n-}\right) = \begin{bmatrix} 0 \\ \overline{\alpha}_i^n \cdot \widehat{\mathbf{F}}_{i-1/2}^{\text{Godunov}} \left(\widehat{\mathbf{U}}_{i-1}^{n+}, \widehat{\mathbf{U}}_i^{n-}\right) \\ \alpha_i^n \cdot \widehat{\mathbf{F}}_{i-1/2}^{\text{Godunov}} \left(\widehat{\mathbf{U}}_{i-1}^{n+}, \widehat{\mathbf{U}}_i^{n-}\right) \end{bmatrix},$$

in the following coupled finite volume scheme:

$$\frac{\mathbf{U}_i^{n+1} - \mathbf{U}_i^n}{\Delta t^n} + \frac{\mathbf{F}_L\left(\mathbf{U}_i^{n+}, \mathbf{U}_{i+1}^{n-}\right) - \mathbf{F}_R\left(\mathbf{U}_{i-1}^{n+}, \mathbf{U}_i^{n-}\right)}{\Delta x} = 0.$$

As for the edge $i+1/2$ the gap in $\bar{\alpha}$ was significant, the Godunov numerical flux for the BN equations (Schwendeman et al., 2006) should be written:

$$\underbrace{\mathbf{F}_L\left(\mathbf{U}_i^{n+}, \mathbf{U}_{i+1}^{n-}\right)}_{\text{full flux}} = \begin{cases} \mathbf{f}\Bigg(\underbrace{\mathbf{U}^*\left[\mathbf{U}_i^{n+}, \mathbf{U}_{i+1}^{n-}\right]}_{\text{Riemann problem solution}}\Bigg) - \underbrace{\mathbf{H}\left(\mathbf{U}_i^{n+}, \mathbf{U}_{i+1}^{n-}\right)}_{\text{non-conservative part of the full flux}}, & \text{if } \overline{v}_{c,i+1/2}^n < 0, \\ \underbrace{\mathbf{f}\left(\mathbf{U}^*\left[\mathbf{U}_i^{n+}, \mathbf{U}_{i+1}^{n-}\right]\right)}_{\text{conservative part of the full flux}}, & \text{if } \underbrace{\overline{v}_{c,i+1/2}^n}_{\text{velocity of the solid contact}} > 0, \end{cases} \quad (13)$$

$$\underbrace{\mathbf{F}_R\left(\mathbf{U}_i^{n+}, \mathbf{U}_{i+1}^{n-}\right)}_{\text{full flux}} = \begin{cases} \mathbf{f}\left(\mathbf{U}^*\left[\mathbf{U}_i^{n+}, \mathbf{U}_{i+1}^{n-}\right]\right), & \text{if } \overline{v}_{c,i+1/2}^n < 0, \\ \mathbf{f}\left(\mathbf{U}^*\left[\mathbf{U}_i^{n+}, \mathbf{U}_{i+1}^{n-}\right]\right) + \mathbf{H}\left(\mathbf{U}_i^{n+}, \mathbf{U}_{i+1}^{n-}\right), & \text{if } \overline{v}_{c,i+1/2}^n > 0. \end{cases} \quad (14)$$

The non-conservative part of the full flux is calculated using the relation below:

$$\mathbf{H}\left(\mathbf{U}_i^n, \mathbf{U}_{i+1}^n\right) = \begin{bmatrix} -\bar{v}_{c,i+1/2}^n\left(\bar{\alpha}_{i+1}^n - \bar{\alpha}_i^n\right) \\ 0 \\ \bar{p}_{i+1}^n\bar{\alpha}_{i+1}^n - \bar{p}_i^n\bar{\alpha}_i^n \\ \bar{v}_{c,i+1/2}^n\left(\bar{p}_{i+1}^n\bar{\alpha}_{i+1}^n - \bar{p}_i^n\bar{\alpha}_i^n\right) \\ 0 \\ -\left(\bar{p}_{i+1}^n\bar{\alpha}_{i+1}^n - \bar{p}_i^n\bar{\alpha}_i^n\right) \\ -\bar{v}_{c,i+1/2}^n\left(\bar{p}_{i+1}^n\bar{\alpha}_{i+1}^n - \bar{p}_i^n\bar{\alpha}_i^n\right) \end{bmatrix}. \quad (15)$$

If both conditions (9) were not valid, the numerical fluxes for both edges were calculated using (13), (14). The key point was the construction of the Riemann problem solution $\mathbf{U}^*[.,.]$. In turn, it also contained two distinct cases, namely the case of solid phase existence from both sides of the edge (see Fig. 2a) and solid phase vanishing case (see Fig. 2b).

The algorithm of the Riemann problem solution $\mathbf{U}^*$ for the states $\mathbf{U}_L$ and $\mathbf{U}_R$ from different sides of the discontinuity included:

- Finding initial guesses for the gas and solid pressures, gas and solid velocities at the solid contact from the solution of the classical single-phase Riemann problems $\widehat{\mathbf{U}}^*(\widehat{\mathbf{U}}_L, \widehat{\mathbf{U}}_R)$ and $\widehat{\mathbf{U}}^*(\widehat{\mathbf{U}}_L, \widehat{\mathbf{U}}_R)$;
- Iterative solution of the system of four (the case from Fig. 2a) or three (the case from Fig. 2b) non-linear algebraic equations using Newton solver to find gas and solid pressures to the left and to the right from the discontinuity. In the case from Fig. 2b, the solid phase vanished in the cell $i+1$ so the solid phase pressure here did not have the physical meaning. So, the system of three equations to find solid phase pressure to the left and gas pressure to the left and to the right of the discontinuity was solved. Velocity of the solid contact that was used in (13)– (15) was also found. The systems of non-linear algebraic equations and their Jacobians are written in the Appendix;
- Sampling the total solution of the Riemann problem in gas and solid phases.

For more details, our C++ code is available (Computer Code for the Godunov Solver, 2020). It is not the constituent part of the whole code directly, but it is a clarified and extensively commented Toro-like code for the solution of a single Riemann problem for the BN equations, implemented for the case of a solid phase volume fraction gap when solid phase exists on both sides of the initial discontinuity (the case from Fig. 2a).

The accuracy of the numerical method in the hyperbolic step in time is equal to unity due to the explicit Euler time integration scheme. The overall accuracy of the numerical algorithm is also equal to unity because of the properties of the Strang splitting scheme (7) (Toro, 2009). The overall accuracy of the numerical algorithm in space is equal to two on smooth solutions due to the properties of minmod reconstruction (Toro, 2009).

3.2. Relaxation procedure and algebraic source terms

For the simulation of reversible loading of the layer the stiff pressure relaxation was realized. Initially in (Baer and Nunziato, 1986) the finite rate of pressure relaxation was defined by the term F in (1). Transition to (2) was carried out under the assumption of $\mu_c \to 0$ and so the specific value of μ_c was not necessary for the stiff pressure relaxation. The following system of ordinary differential equations was solved:

$$\begin{cases} \frac{d\alpha}{dt} = -F, \\ \frac{d(\alpha\rho)}{dt} = 0, \\ \frac{d(\alpha\rho v)}{dt} = 0, \\ \frac{d(\alpha\rho E)}{dt} = pF, \\ \frac{d(\bar{\alpha}\bar{\rho})}{dt} = 0, \\ \frac{d(\bar{\alpha}\bar{\rho}\bar{v})}{dt} = 0, \\ \frac{d(\bar{\alpha}\bar{\rho}\bar{E})}{dt} = -(p+\beta)F. \end{cases} \quad (16)$$

From the second, the third, the fifth and the sixth equations of (16) velocities of the solid and gas phases remained constant at this stage. Using this fact and the first equation the fourth and the seventh equations were rewritten as:

$$\frac{d(\alpha\rho e)}{dt} = -p\frac{d\alpha}{dt}, \quad \frac{d(\bar{\alpha}\bar{\rho}\bar{e})}{dt} = -(p+\beta)\frac{d\alpha}{dt}.$$

The consequences of the second and fifth equations were:

$$\frac{d\alpha}{dt} = -\frac{\alpha}{\rho}\frac{d\rho}{dt}, \quad \frac{d\bar{\alpha}}{dt} = -\frac{\bar{\alpha}}{\bar{\rho}}\frac{d\bar{\rho}}{dt}.$$

Then the fourth and seventh equations became:

$$\frac{de}{dt} = -p\frac{d}{dt}\left(\frac{1}{\rho}\right), \quad \frac{d\bar{e}}{dt} = -(p+\beta)\frac{d}{dt}\left(\frac{1}{\bar{\rho}}\right).$$

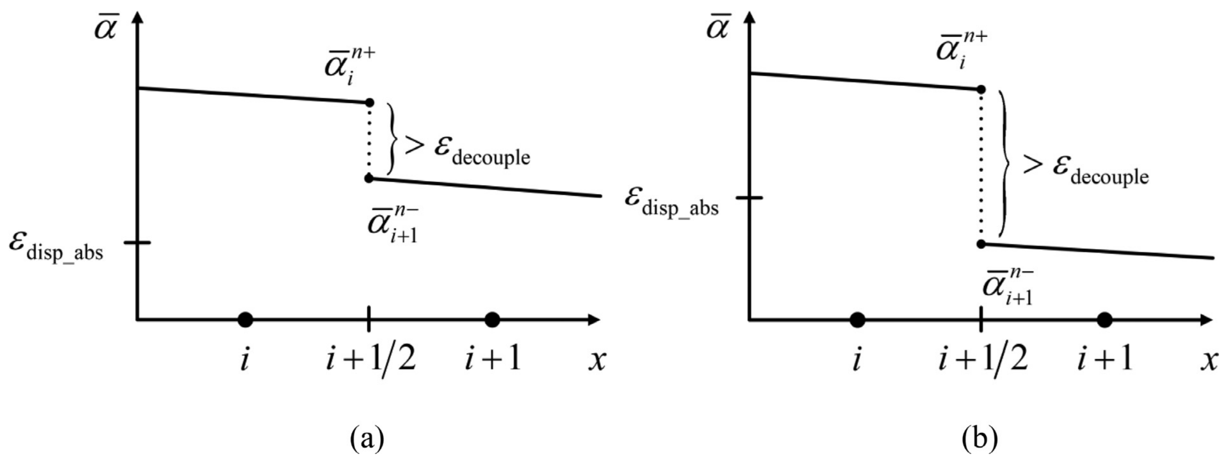

Fig. 2. The schematic of the case of a solid phase volume fraction gap: (a) solid phase exists from the both sides from the edge; (b) solid phase vanishing case.

After the discretization and approximation of the derivatives (Saurel and Lemetayer, 2001) these equations were written in the following way:

$$\begin{cases} e^{n+1}-e^n = -\frac{1}{2}\left(p^{n+1}+p^n\right)\left(\frac{1}{\rho^{n+1}}-\frac{1}{\rho^n}\right),\\ \bar{e}^{n+1}-\bar{e}^n = -\frac{1}{2}\left(p^{n+1}+\beta^{n+1}+p^n+\beta^n\right)\left(\frac{1}{\bar{\rho}^{n+1}}-\frac{1}{\bar{\rho}^n}\right).\end{cases}$$

The usage of the stiffened gas EOS for the particles and for the gas phase led to the following system of non-linear algebraic equations to find p^{n+1}, ρ^{n+1} and $\bar{\rho}^{n+1}$:

$$\begin{cases} \frac{p^{n+1}+\gamma\pi_0}{\rho^{n+1}(\gamma-1)}-\frac{p^n+\gamma\pi_0}{\rho^n(\gamma-1)} = -\frac{1}{2}\left(p^{n+1}+p^n\right)\left(\frac{1}{\rho^{n+1}}-\frac{1}{\rho^n}\right),\\ \frac{p^{n+1}+\beta^{n+1}+\bar{\gamma}\bar{\pi}_0}{\bar{\rho}^{n+1}(\bar{\gamma}-1)}-\frac{\bar{p}^n+\bar{\gamma}\bar{\pi}_0}{\bar{\rho}^n(\bar{\gamma}-1)} = -\frac{1}{2}\left(p^{n+1}+\beta^{n+1}+p^n+\beta^n\right)\\ \left(\frac{1}{\bar{\rho}^{n+1}}-\frac{1}{\bar{\rho}^n}\right),\\ \frac{\alpha^n\rho^n}{\rho^{n+1}}+\frac{\bar{\alpha}^n\bar{\rho}^n}{\bar{\rho}^{n+1}} = 1. \end{cases} \tag{17}$$

Here the constraint $\alpha^{n+1}+\bar{\alpha}^{n+1}=1$ was also taken into account. The system then was reduced to one non-linear equation with the unknown $\bar{\rho}^{n+1}$ which was solved numerically using Newton's iterations:

$$\bar{\rho}_{j+1}^{n+1} = \bar{\rho}_j^{n+1}-\varphi(\bar{\rho}_j^{n+1})/\varphi'(\bar{\rho}_j^{n+1}),$$

$$\varphi\left(\bar{\rho}_j^{n+1}\right) = \frac{p_j^{n+1}+\beta\left(\bar{\rho}_j^{n+1}\right)+\bar{\gamma}\bar{\pi}_0}{(\bar{\gamma}-1)\bar{\rho}_j^{n+1}}-\frac{\bar{p}^n+\bar{\gamma}\bar{\pi}_0}{(\bar{\gamma}-1)\bar{\rho}^n} + \frac{1}{2}\left(p_j^{n+1}+\beta\left(\bar{\rho}_j^{n+1}\right)+p^n+\beta\left(\bar{\rho}^n\right)\right)\left(\frac{1}{\bar{\rho}_j^{n+1}}-\frac{1}{\bar{\rho}^n}\right), \tag{18}$$

$$\begin{aligned}\varphi'\left(\bar{\rho}_j^{n+1}\right) = {} & \frac{1}{\bar{\rho}_j^{n+1}(\bar{\gamma}-1)}\left(\frac{dp_j^{n+1}}{d\bar{\rho}_j^{n+1}}+\frac{d\beta\left(\bar{\rho}_j^{n+1}\right)}{d\bar{\rho}_j^{n+1}}\right)\\ & -\frac{p_j^{n+1}+\beta\left(\bar{\rho}_j^{n+1}\right)+\bar{\gamma}\bar{\pi}_0}{\left(\bar{\rho}_j^{n+1}\right)^2(\bar{\gamma}-1)}\\ & -\frac{1}{2\left(\bar{\rho}_j^{n+1}\right)^2}\left(p_j^{n+1}+\beta\left(\bar{\rho}_j^{n+1}\right)+p^n+\beta\left(\bar{\rho}^n\right)\right)\\ & +\frac{1}{2}\left(\frac{dp_j^{n+1}}{d\bar{\rho}_j^{n+1}}+\frac{d\beta\left(\bar{\rho}_j^{n+1}\right)}{d\bar{\rho}_j^{n+1}}\right)\left(\frac{1}{\bar{\rho}_j^{n+1}}-\frac{1}{\bar{\rho}^n}\right),\end{aligned}$$

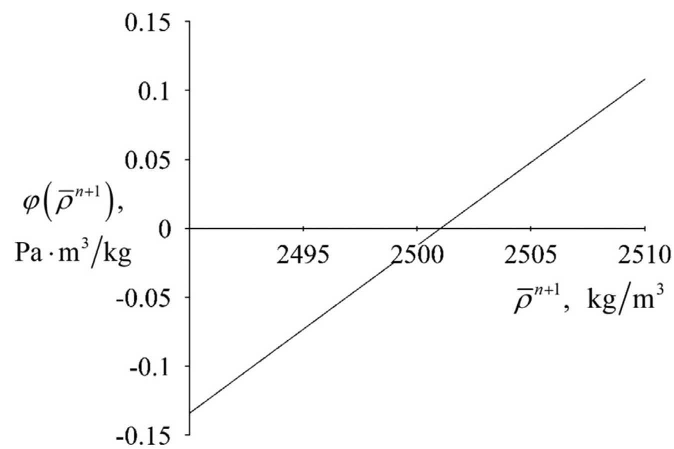

Fig. 3. The typical view of φ function (18) in verification simulation from Section 4.2 The time instant is 560 μs, $x = 1.4$m.

where j denotes iterations index and

$$p_j^{n+1}\left(\bar{\rho}_j^{n+1}\right) = \frac{\frac{1}{\rho_j^{n+1}}\left(-\frac{\gamma\pi_0}{\gamma-1}-\frac{p^n}{2}\right)+\frac{p^n+\gamma\pi_0}{(\gamma-1)\rho^n}+\frac{p^n}{2\rho^n}}{\frac{1}{\rho_j^{n+1}}\cdot\frac{\gamma+1}{2(\gamma-1)}-\frac{1}{2\rho^n}},\ \rho_j^{n+1}\left(\bar{\rho}_j^{n+1}\right) = \left(\frac{1}{\alpha^n\rho^n}-\frac{1}{\bar{\rho}_j^{n+1}}\cdot\frac{\bar{\alpha}^n\bar{\rho}^n}{\alpha^n\rho^n}\right)^{-1}.$$

Parameters calculated on the previous stage of the Strang splitting scheme were taken as initial values in Newton's iterations. It can be seen from Fig. 3 that Eq. (18) had only one possible solution for the range of parameters typical for the considered problem. The root of φ function in general was found within 1-2 iterations with the accuracy at least $|(\bar{\rho}_{j+1}^{n+1}-\bar{\rho}_j^{n+1})/\bar{\rho}_j^{n+1}| = 10^{-7}$. Then the rest parameters were found:

$v^{n+1} = v^n$, $\bar{v}^{n+1} = \bar{v}^n$, $\bar{p}^{n+1} = p^{n+1}+\beta^{n+1}$, $\alpha^{n+1} = \alpha^n\rho^n/\rho^{n+1}$, $\bar{\alpha}^{n+1} = 1-\alpha^{n+1}$.

For the simulation of an irreversible compaction of the particles the system (17) was solved only if $\bar{p}^n > p^n+\beta^n$ and $\bar{\alpha}^n > \varepsilon_{\text{disp\_abs}}$. Otherwise the compaction with the finite rate F was taken into account at the final stage L_s of the splitting procedure (7).

The final stage of the numerical algorithm took into account the physical processes described by the algebraic source terms in the vector **s** and possibly vector **p** in case of irreversible compaction in (1). The solution from the previous pressure relaxation step was taken as the initial condition. The system of ordinary differential equations was solved numerically using explicit Euler scheme.

4. Verification

4.1. Riemann problem

The Riemann problem for the reduced BN equations (without **p** and **s** terms in (1)) from (Schwendeman, 2006) was considered as a test for the non-vanishing solid phase case. Computational domain was a segment [0;1]. Non-penetrating conditions were imposed at the boundaries. The following dimensionless parameters were used as the initial data to the left and to the right of discontinuity at $x = 0.5$:

$$\bar{\alpha}_{\rm L} = 0.8,\ \bar{\rho}_{\rm L} = 1.0,\ \bar{v}_{\rm L} = 0.0,\ \bar{p}_{\rm L} = 1.0,\ \rho_{\rm L} = 0.2,\ v_{\rm L} = 0.0,\ p_{\rm L} = 0.3,$$

$$\bar{\alpha}_{\rm R} = 0.3,\ \bar{\rho}_{\rm R} = 1.0,\ \bar{v}_{\rm R} = 0.0,\ \bar{p}_{\rm R} = 1.0,\ \rho_{\rm R} = 1.0,\ v_{\rm R} = 0.0,\ p_{\rm R} = 1.0.$$

CFL number was equal to 0.8. This test case is available as a sample in our computer code (Computer Code for the Godunov Solver, 2020). Fig. 4 shows the convergence of the numerical solution to the exact one with grid refinement.

4.2. Rogue shock tube

In our previous study (Utkin, 2017), (Utkin, 2019), we focused on the parametric numerical simulation of a SW – particles cloud interaction problem (Rogue et al., 1998) using the HLL method (Saurel and Abgrall, 1999) and the Godunov method (Schwendeman, 2006). Unlike previous work, intergranular stresses in the solid phase were taken into account in the stiff pressure relaxation procedure here. Similar to (Saurel et al., 2010), we did not take into account irreversible compaction of particles here.

The statement of the problem corresponded to the full-scale experiment (Rogue et al., 1998) and was the same as in (Utkin, 2017) and (Utkin, 2019). A SW with Mach number $M = 1.3$ interacted with a cloud of glass spherical particles of the diameter $d = 1.5\,\text{mm}$ and the initial volume fraction $\bar{\alpha}_0 = 0.65$. The initial true density of particles was $\bar{\rho}_0 = 2500\text{kg/m}^3$. The length of the computational domain was 2.8 m. The left boundary of the domain was $x = 0$. The coordinate of the left boundary of the cloud of particles was equal to $x_L = 1.39$m, the coordinate of the right boundary was $x_R = 1.41$m. At the initial time moment a SW was located at the point with the coordinate x_R that is at the right boundary of the cloud and moved from the right to the left. The gas pressure was recorded with the use of three transducers located at the points with the coordinates $x_1 = 0.692$m, $x_2 = 1.367$m (downstream transducers) and $x_3 = 1.520$m (upstream transducer). At the initial time moment the area $[0; x_R]$ was filled with the quiescent air under the normal conditions. The non-penetrating condition was set at the left boundary, the inflow condition with the parameters behind the SW with Mach number 1.3 was set at the right boundary. The simulation time was 4 ms and corresponded to the compression phase duration behind the incident SW in the experiments (Rogue et al., 1998). Parameters in (3)– (6) used in the simulation were close to (Saurel et al., 2010):

$\bar{\alpha}_{\rm crit} = \bar{\alpha}_0$, $a = 3 \cdot 10^4\,\text{J/kg}$, $n = 1.02$.

Parameters in the stiffened gas EOS for the solid phase were the following (Utkin, 2017):

$$\overline{\gamma} = 2.5 \text{ and } \overline{\pi}_0 = 10^8\,\text{Pa}. \tag{19}$$

In our simulation, a cells number was equal to 22 400, CFL number was equal to 0.5.

The evolution of the solid phase volume fraction at the initial time moments was analyzes for both cases – with and without intergranular stresses. Interaction of an incident SW with a cloud led to the CW in the solid phase and filtration wave in gas. Fig. 5, left illustrates the dynamics of the forward propagation of the CW along the particles cloud.

After that a CW interacted with a free boundary of the cloud, reflected from it and propagated to the right followed by some kind of the analogue of solid phase rarefaction wave. Up to the time instant of about 0.15 ms, a maximal solid phase volume fraction decreased below $\bar{\alpha}_{\rm crit}$ and from that time configuration pressure was equal to zero. Fig. 6 demonstrates the comparison of simulations with and without intergranular stresses. The increase of $\bar{\alpha}$ up to 0.672 was observed in the case without intergranular stresses in contrast to about 0.652 in the case with intergranular stresses. At the same time the leading edge of the “compacted” cloud moved at longer distance (see Fig. 6b). Interaction of the incident SW with the dense particles cloud led to the formation of the reflected and transmitted waves (see Fig. 7). Pressure transducers No. 1 and 2 detected a transmitted wave, transducer No. 3 – a reflected wave. The relative error in comparison with the experimental data for the transducers No. 2 and 3 did not exceed 3%. The simulation correctly reproduced the change in the rate of pressure curve growth on the transducer No. 2 at a time of about 2.5 which was associated with the passage of a cloud of particles through the point at which the transducer was installed. On the transducer No. 1, the maximum relative error was about 5%. The influence of the intergranular stresses on the intensities of transmitted and reflected waves appeared to be negligibly small although the dynamics of cloud motion was more relevant from the physical point of view at the initial stages of the process in the simulation with intergranular stresses.

The leading edge of the cloud remained very sharp due to the usage of the Godunov method (see Fig. 6). Its thickness in terms of computational cells increases from approximately 5 at the time moment 0.2 ms to approximately 20 at the time moment 1.4 ms. It was shown in (Utkin, 2019) that the usage of the HLL method led to about 5 times greater spatial smearing of the leading front of the cloud at the final time 4 ms as well as the lowering the maximal solid phase volume fraction in the cloud up to about 0.3 instead of 0.5 in the simulation using the Godunov scheme.

5. Interaction of a shock wave with a layer of particles near a rigid wall

5.1. Statement of the problem

Statement of the problem corresponded to the full-scale experiments (Gelfand et al., 1989). Experiments were performed in a vertical shock tube 3 m long. It consisted of a high-pressure chamber filled with nitrogen or helium which was separated from the low-pressure chamber filled with air under normal conditions by a diaphragm. As a diaphragm was removed, a SW was generated and it interacted with a layer of polystyrene particles 20 mm thick (see Fig. 8). The diameter of the particles was 0.2 mm and the initial volume fraction of particles constituted 0.48. The low-pressure chamber was equipped with several pressure transducers. We were interested in the wall pressure under the particles layer. Therefore, the data from the correspondent transducer was reproduced in the simulations.

Similar to Section 4.2, we consider a one-dimensional frame of reference Ox. Point O corresponded to the left boundary of the computational domain with a length of 0.37 m. The coordinate of the left boundary of the spherical particles layer was $x_L = 0.35$m, while the coordinate of the right boundary coincided with the right end of the computational domain and constituted $x_R = 0.37$ m. The initial true density of the solid phase was $\bar{\rho}_0 = 1060\text{kg/m}^3$. At the initial time moment the SW was located at the point with the coordinate $x_S = x_L$ and moved from the left to the right. The area $[x_S; x_R]$ was initially filled with the quiescent air (the specific heat ratio was $\gamma = 1.4$, $\pi_0 = 0$) with the density $\rho_0 = 1.2\,\text{kg/m}^3$ and under the pressure $p_0 = 10^5\,\text{Pa}$. In the area $[0; x_S]$, we set pa-

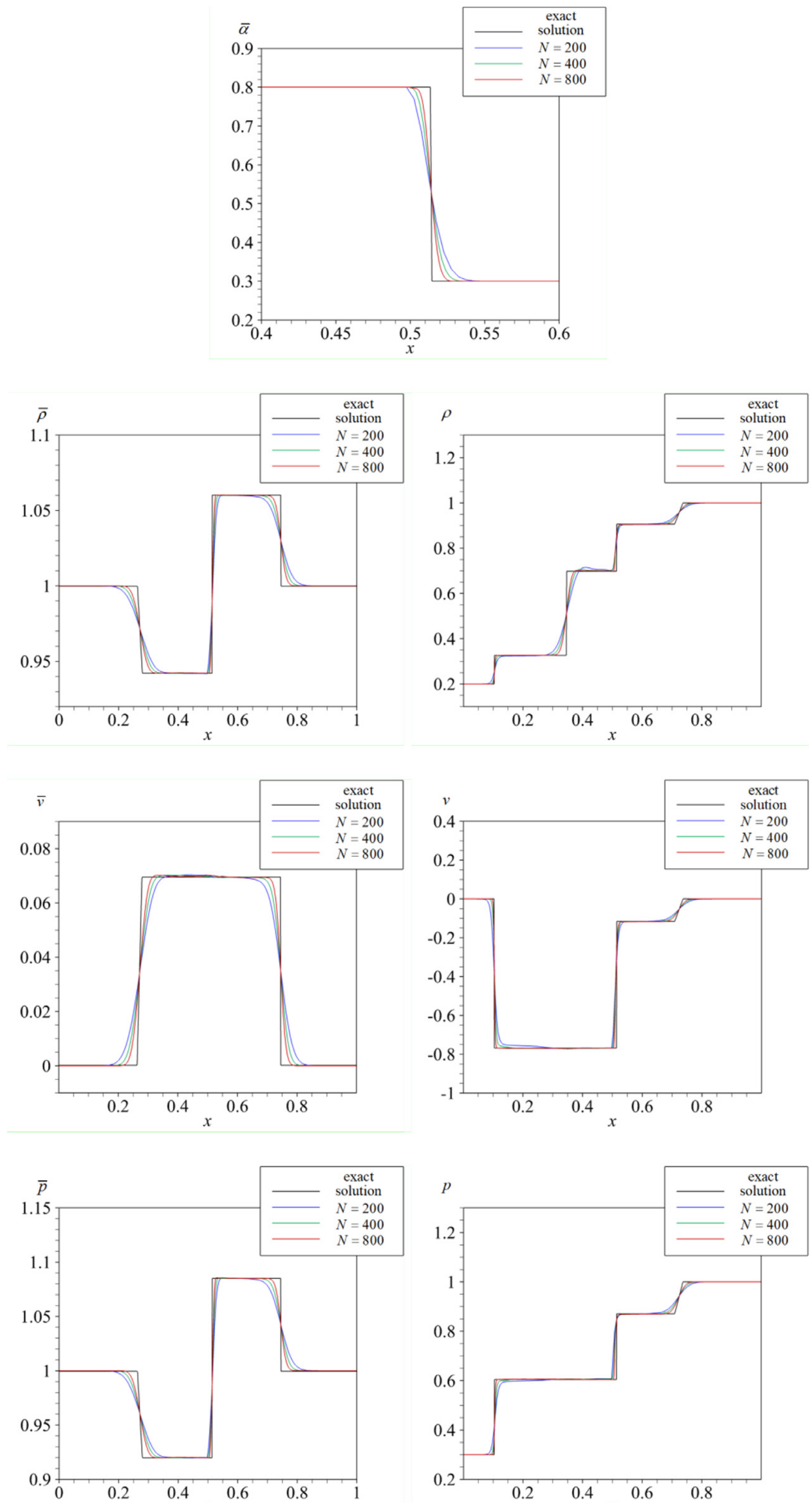

Fig. 4. Solution of the Riemann problem for the reduced BN equations using the Godunov method (second order in space) on three different grids in comparison with the exact solution.

rameters behind the SW with a Mach number $M = 1.36$ propagating in the positive direction of the axis Ox:

$\rho_M = 1.95\,\mathrm{kg/m^3}$, $v_M = 179.97\,\mathrm{m/s}$ and $p_M = 2.00 \cdot 10^5\,\mathrm{Pa}$.

The non-penetrating condition was set at the right boundary, the inflow condition with the parameters ρ_M, v_M and p_M was set at the left boundary. Parameters of the solid phase stiffened-gas EOS were the same as in the Rogue test. The influence of those parameters in the considered problem of SW– particles layer interaction was very small, see Section 5.2. As a result of another parametric study (see also Section 5.2), the following parameters in the intergranular stresses model (2) – (6) were chosen:

$$\overline{\alpha}_{\mathrm{crit}} = 0.48,\ a = 10^5\,\mathrm{J/kg},\ n = 1.02.$$

The variation started with the basic parameters from (Saurel et al., 2010) that were obtained from the analysis of

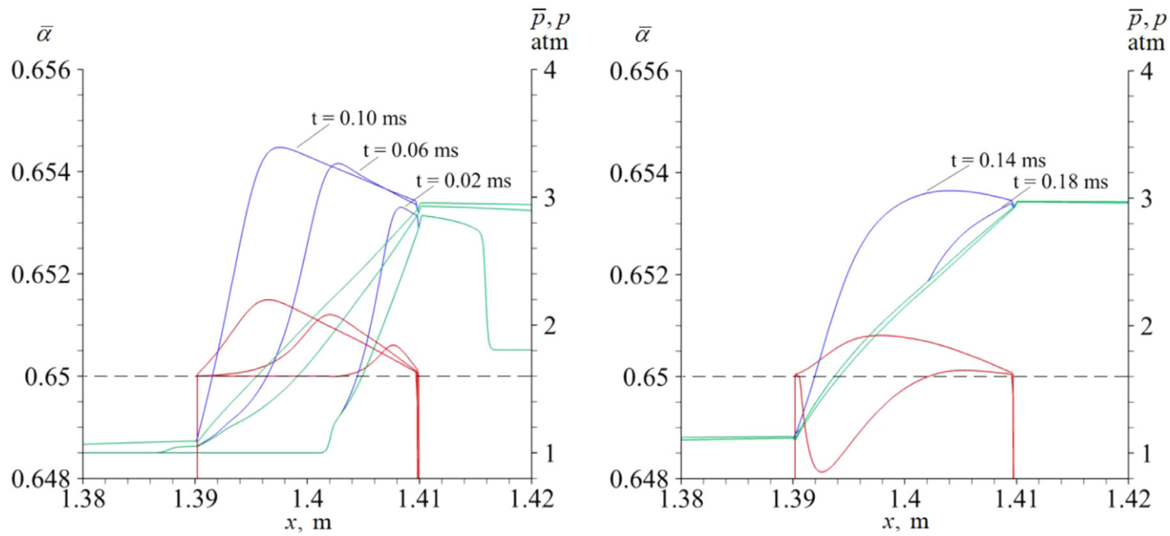

Fig. 5. Predicted spatial distributions of the solid phase volume fraction (red lines), pressure of the solid (blue lines) and the gas (green lines) phases at the successive time moments in the simulation with intergranular stresses. Here and further the black dashed line denotes $\bar{\alpha}_{\text{crit}}$ level in (4).

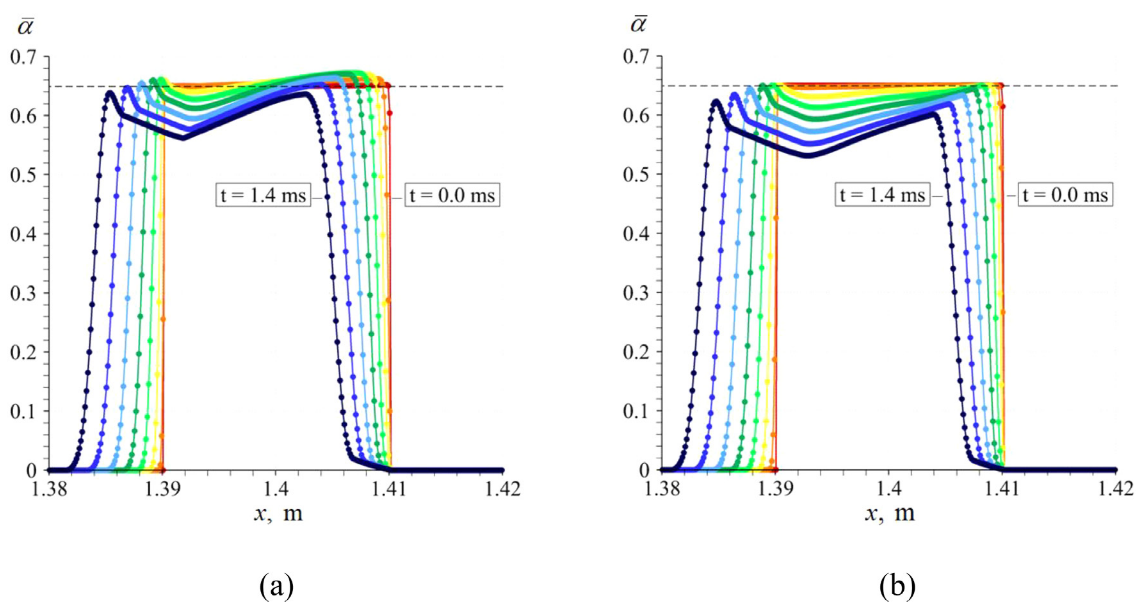

Fig. 6. Predicted spatial distributions of the solid phase volume fraction at the successive time moments with a gap 0.2 ms: (a) without intergranular stresses; (b) with intergranular stresses. Dots denote computational cell centers.

experiments on compression of HMX and NaCl in the pressure range of 0.1 – 25 MPa. Computational cell grid size was equal to $\Delta x = 0.125$ mm.

Experiments (Gelfand et al., 1989) were also simulated in (Kutushev and Rudakov, 1993) and (Fedorov and Fedorchenko, 2005). The latter one used a dusty gas mathematical model and therefore the simulation of this problem was carried out with a volume fraction of particles being equal to 0.015. For this reason, the effects of intergranular stresses in the solid phase were not taken into account, and, in fact, only waves in the gas phase were described. In (Kutushev and Rudakov, 1993), R.I. Nigmatulin model (Nigmatulin, 1990) was used. The model took into account intergranular stress in the phase of particles. The model of intergranular stresses was more complex than (3) – (6), but also had a threshold form. Further, the obtained results will be compared to the data from (Kutushev and Rudakov, 1993).

5.2. Results: reversible loading-unloading of the layer

Initially, the problem was considered using the stiff pressure relaxation everywhere. Normally incident SW interacted with the particles layer that led to the formation of reflected wave propagated upstream in the pure air (see Fig. 9a). Gas penetrated inside the layer as a compression wave with a smeared front. CW propagated in the solid phase. Its movement to the right across the layer was accompanied by the increase of the solid phase volume fraction and, hence, the origin of the configuration pressure.

The period of time from $t \approx 0.06$ ms to $t \approx 0.14$ ms corresponded to the sharp rise of the configuration pressure and hence the mixture pressure $p_{\text{mix}} = \alpha p + \bar{\alpha}\bar{p}$ at the rigid wall. This mixture pressure was compared to the experimental data from the pressure transducer (see Fig. 10). Also the particles layer as a whole was compressed, the interface boundary shifted to the right. At $t \approx 0.14$ ms a CW reflected from the wall and started moving towards the interfacial boundary (see Fig. 9b). At this time the solid phase volume fraction began decreasing gradually near the wall

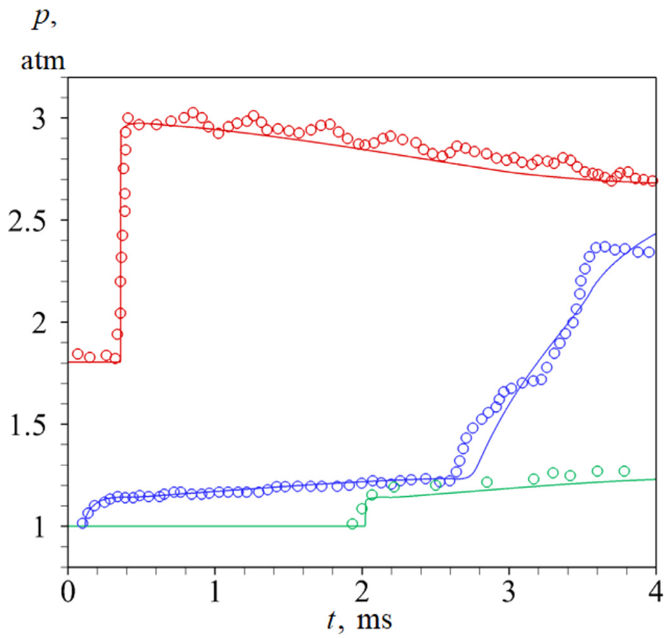

Fig. 7. Comparison of the predicted (solid lines) and the experimental (Roguet et al., 1998) (dots) pressure curves on three transducers: green color– transducer No. 1, blue color– transducer No. 2, red color– transducer No. 3.

and it brought about the steady decline of the p_{mix} (see Fig. 10). At $t \approx 0.22$ ms the CW reflected from the interfacial boundary and moved towards the wall while the volume fraction of the solid phase continued to decrease near the wall. The interface boundary changed the direction of its motion. Starting from $t \approx 0.3$ ms the solid phase volume fraction became less than $\bar{\alpha}_{crit}$ near the wall, intergranular pressure did not work any longer ($\beta = 0$) and, according to the equilibrium condition (2), $\bar{p} = p$ (see Fig. 10).

We interpreted the experimental data from (Gelfand et al., 1989) as an oscillating curve with a pronounced first peak, which was characterized by specific values of its amplitude and width. The experimental curve also reached a certain average value over time. Predicted solid phase pressure as well as p_{mix} were characterized by the first jump associated with the arrival of the CW. The difference in the amplitude of this jump was approximately 15% in comparison with the experimental value. The experimental and predicted width of the peak correlated reasonably. There was also a correspondence in the level which all pressure curves eventually reached. At the same time the model with stiff pressure relaxation with considered parameters did not provide the oscillations after the first pressure peak. Such oscillations are visible on the experimental curve. So we continued the parametric study of the solid phase EOS and intergranular stresses model parameters influence on the simulation results.

Polystyrene at pressures of the order of GPa is described by the Mie-Gruneisen EOS (Khishchenko et al., 1996), the longitudinal speed of sound in this material is about 2350 m/s (Handbook of Chemistry and Physics, 2005). For the used stiffened gas EOS, for the solid phase such speed of sound was obtained for the parameters $\bar{\gamma} = 2.5$, $\bar{\pi}_0 \approx 2.6 \cdot 10^9$ Pa. Parameters (19) provided the speed of sound 485 m/s under the normal conditions. However, Fig. 11 demonstrates that the value of $\bar{\pi}_0$ influenced the pressure curve under the layer insignificantly. The greatest effect here was the significant decrease of the integration time step (12). Similar effects were observed in (Utkin, 2017). Weak dependence of the results on the EOS parameters of the solid phase was determined by the fact that polystyrene was almost incompressible within this problem. However, nominal compressibility of both phases is an important feature of the considered BN model that ensures its hyperbolicity.

An increase of parameter $\bar{\alpha}_{crit}$ above an initial value of the solid phase volume fraction in the layer of particles $\bar{\alpha}_0$ led to a later onset of the configuration pressure. In this case, the pressure of the solid phase increased smoothly near the wall, not abruptly in contrast with the experiment (see Fig. 12). Volume fraction of the solid phase increased gradually at the free boundary of the layer, until it exceeded the threshold value $\bar{\alpha}_{crit}$. After that a CW propagated through the layer of particles, and this process was accompanied by an increase in pressure near the wall. The pressure rise was sharper for the greater values of $\bar{\alpha}_{crit}$. The amplitude of the pressure peak also increased. Simulation with $\bar{\alpha}_{crit}$ less than $\bar{\alpha}_0$ caused the decrease of the amplitude of the pressure peak and the increase of its width. Such value of $\bar{\alpha}_{crit}$ implied the existence of the initial intergranular stress not connected with the impact of the SW. This assumption was considered to be non-physical in the analyzed problem.

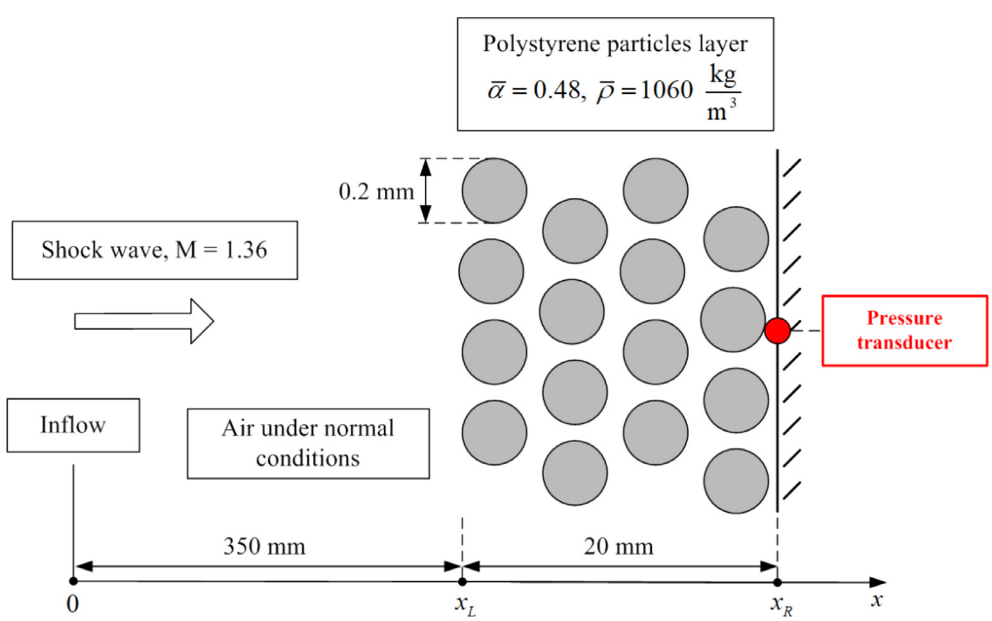

Fig. 8. Schematic of the problem of a SW – particles layer interaction (Gelfand et al., 1989).

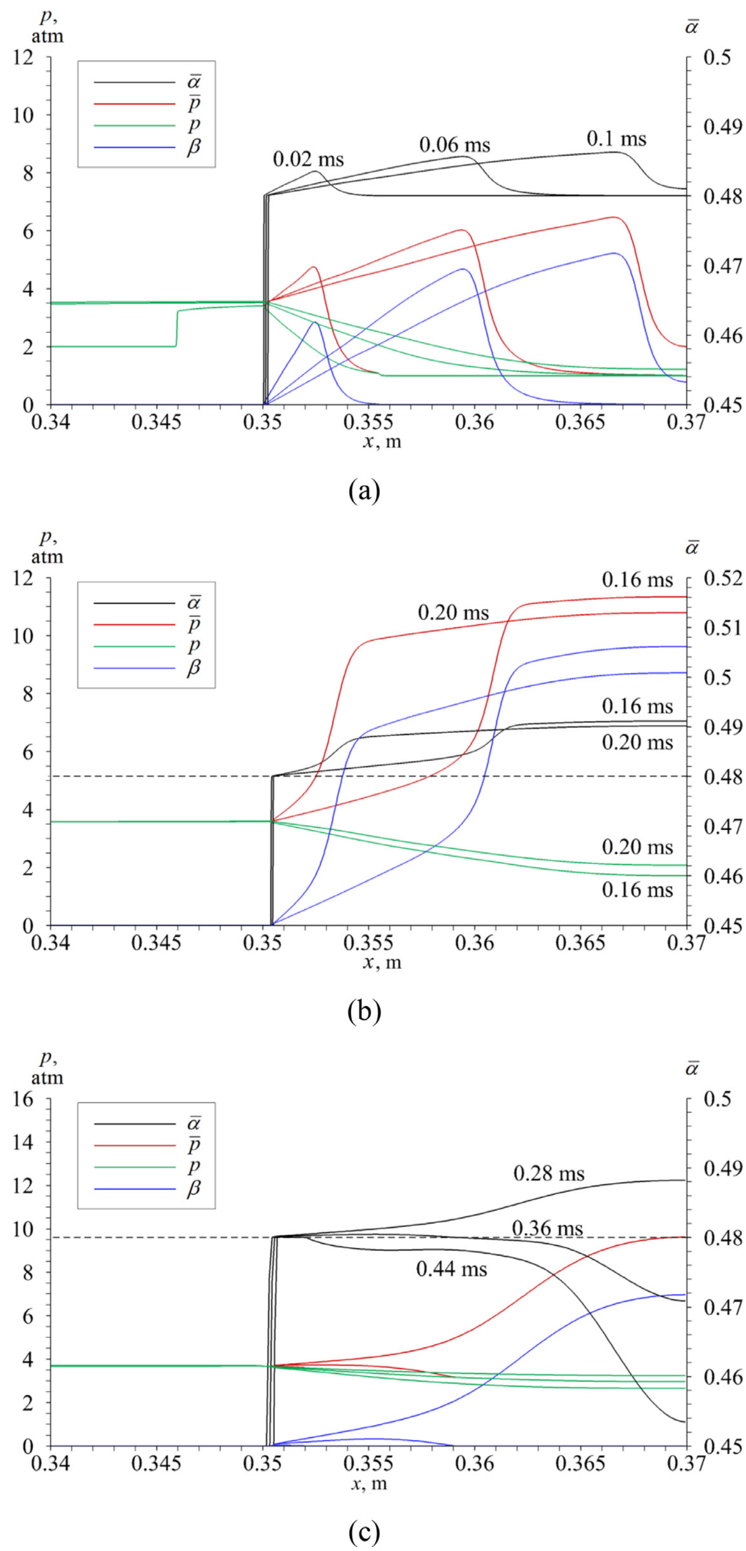

Fig. 9. Predicted spatial profiles of the solid phase volume fraction, solid phase pressure, gas phase pressure and configuration pressure at the successive time moments. The case of reversible loading-unloading process; $\bar{\alpha}_{crit} = 0.48$, $a = 10^5$ J/kg, $n = 1.02$.

Variation of parameter a influenced the maximum pressure near the wall insignificantly. However, it influenced the width of the pressure peak greatly (see Fig. 13). The greater configuration pressure led to the sharper rise of pressure at the moment of arrival of the CW to the wall and to the less gradual decrease of pressure when the CW reflected from the wall. Fig. 14 illustrates qualitatively different case that occurred at the highest value of $a = 5 \cdot 10^5$ J/kg. The first pressure peak did not differ from those disscucced above in principle. However, at about 0.5 ms the secondary peak occurred. The jump of $\bar{\alpha}$ behind the initial CW front appeared to be smaller with the increase of a. It constituted about 10^{-3} for $a = 5 \cdot 10^5$ J/kg in contrast to about $6 \cdot 10^{-3}$ for $a = 10^5$ J/kg

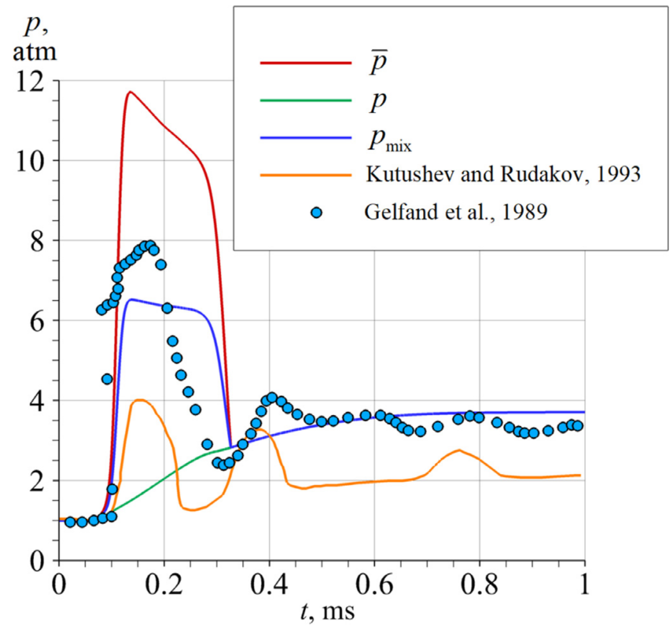

Fig. 10. Comparison of the pressure curves on the wall under the particles layer; $\bar{\alpha}_{crit} = 0.48$, $a = 10^5$ J/kg, $n = 1.02$. The case of reversible loading-unloading process.

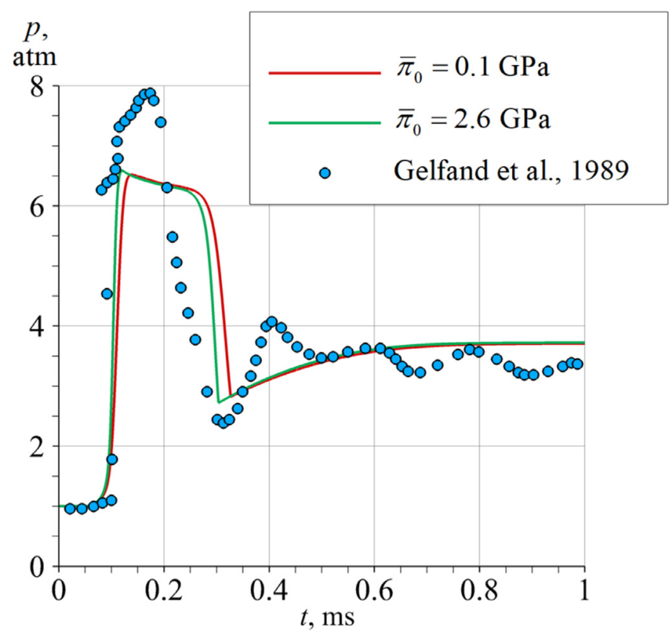

Fig. 11. Effect of parameter $\bar{\pi}_0$ on p_{mix}; $\bar{\alpha}_{crit} = 0.48$, $a = 10^5$ J/kg, $n = 1.02$. The case of reversible loading-unloading process.

(see Fig. 9a). Therefore, during the whole process $\bar{\alpha}$ balanced near the level of $\bar{\alpha}_{crit}$ (see $\bar{\alpha}$ distribution in Fig. 9c at the time of 0.36 ms as a qualitative example) and the mechanism of the second peak formation was connected with the accidental local rise of $\bar{\alpha}$ somewhere inside the layer up to the $\bar{\alpha}_{crit}$ value. The high value of configuration pressure then led to the new CWs propagation in both directions to the wall and interface boundary.

Parameter n in the range $1 + 10^{-6} \le n \le 1.1$ did not affect the width or the amplitude of the pressure peak significantly, as well as the mechanism of CW propagation in the layer.

5.3. Results: irreversible loading-unloading of the layer

Since a true oscillatory nature of the pressure curve on the wall under the layer was not obtained in the "reversible" simulations

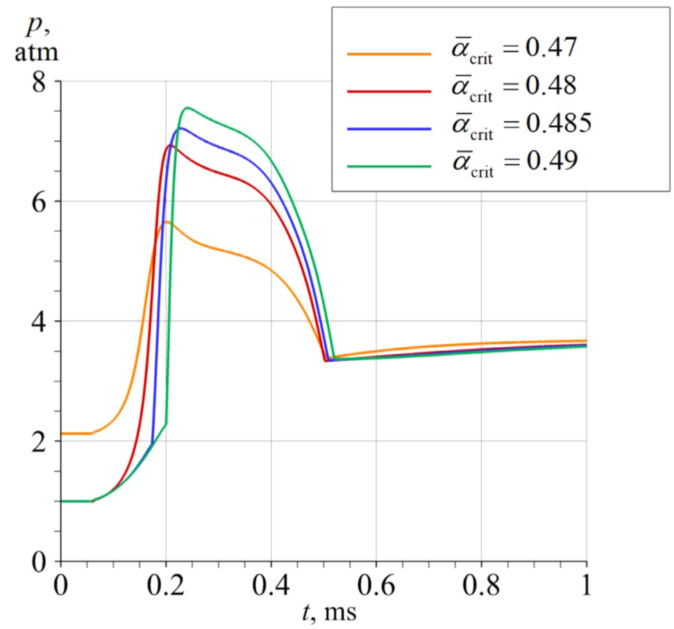

Fig. 12. Effect of parameter $\bar{\alpha}_{crit}$ on p_{mix}; $a = 3 \cdot 10^4$ J/kg, $n = 1.02$. The case of reversible loading-unloading process.

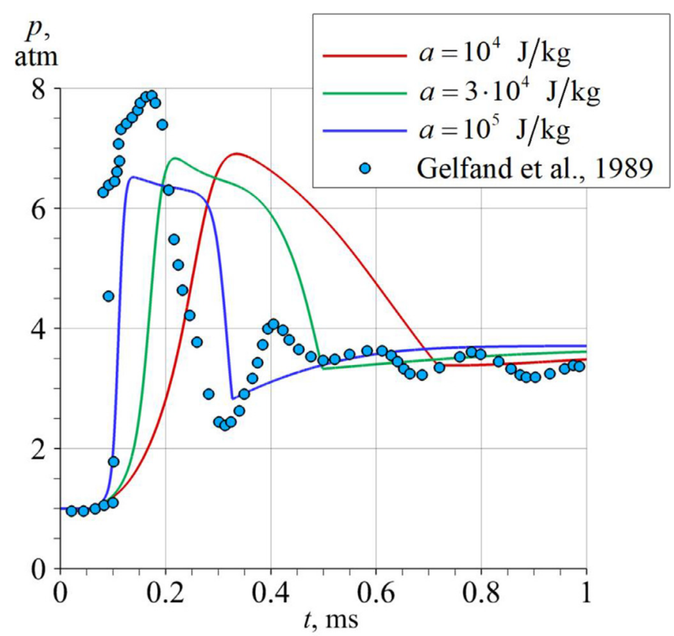

Fig. 13. Effect of parameter a on p_{mix}; $\bar{\alpha}_{crit} = 0.48$, $n = 1.02$. The case of reversible loading-unloading process.

in the previous Section, we proceeded with the irreversible model of a granular layer compaction. In (Saurel et al., 2010) a switch between a stiff pressure relaxation for $\bar{p} > p + \beta$ and $F = 0$ otherwise was proposed. We used a finite compaction rate F with compaction viscosity $\mu = 10^4$ Pa · s instead of $F = 0$.

The same parameters $\bar{\alpha}_{crit} = 0.48$, $a = 10^5$ J/kg, $n = 1.02$ were used as in the basic reversible simulation (see Fig. 9, Fig. 10). Fig. 15 shows that irreversible compaction model provided different shape of the main pressure peak. It became to resemble more the experimental observations. More importantly, irreversible compaction provided oscillations of the pressure curve. The choice $F = 0$ in case $\bar{p} \le p + \beta$ led to the non-damping pressure oscillations so we added compaction viscosity to consideration. Spatial distributions in Fig. 16 clarify the mechanism of oscillations for-

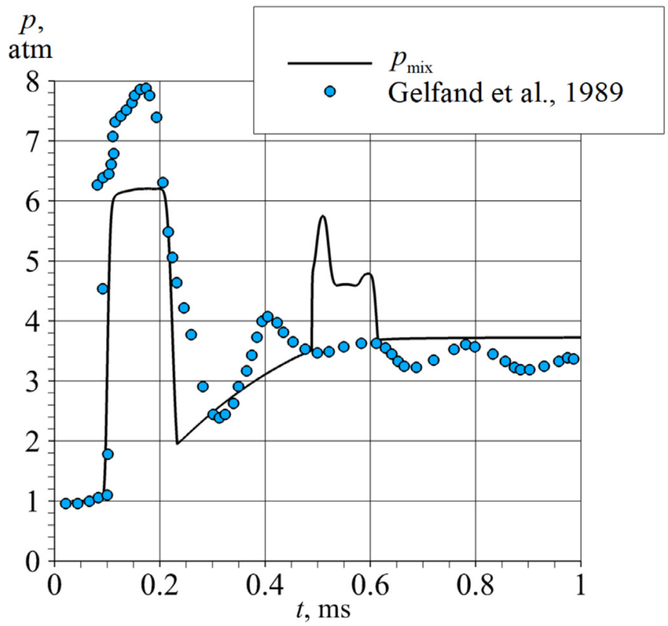

Fig. 14. Predicted wall pressure history for $\bar{\alpha}_{\text{crit}} = 0.48$, $a = 5 \cdot 10^5$ J/kg, $n = 1.02$ in comparison with the experiment. The case of reversible loading-unloading process.

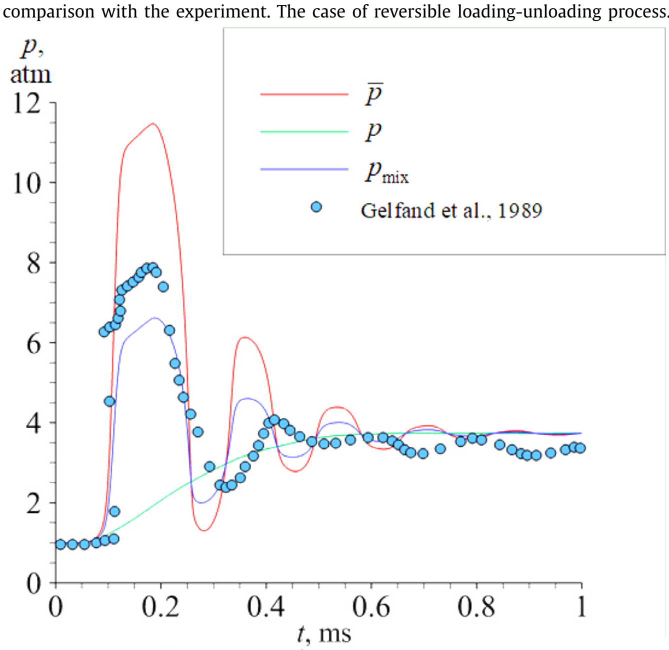

Fig. 15. Predicted wall pressure history for $\bar{\alpha}_{\text{crit}} = 0.48$, $a = 10^5$ J/kg, $n = 1.02$ in comparison with the experiment. Irreversible compaction case.

mation. The main peak was formed in the same manner as in the reversible case, see Fig. 9. However, after the reflection of a CW from the wall the solid phase volume fraction near the wall did not decrease as fast as in the reversible case. Consequently, configuration pressure also remained nearly constant near the wall. In such situation, the sources of oscillations are the pressure waves in the solid phase that travel between the wall and the free boundary of the layer with gradual damping.

6. Nowadays

The models based on the BN equations and on the kinetic theory of granular media (KTGM) (Gidaspow, 1994) are among the most developed and widespread for the simulations of high-speed dense flows of two-phase media. Applied to the considered problem, these two classes of equations have the following difference (Houim and Oran, 2016). In the approach based on the BN equations, one of the equations of the governing system is the compaction equation, the first equation of system (1), which has the following form without the right-hand side term:

$$\frac{\partial \bar{\alpha}}{\partial t} + \bar{v}\frac{\partial \bar{\alpha}}{\partial x} = 0. \tag{20}$$

It should be reminded that the BN model implies the compressibility of both the gas and the solid phases. KTGM contains different equation for $\bar{\alpha}$ evolution considering the particles phase incompressible:

$$\frac{\partial \bar{\alpha}}{\partial t} + \frac{\partial}{\partial x}(\bar{\alpha}\bar{v}) = 0. \tag{21}$$

The mathematical structure of Eqs. (20) and (21) is different. The Eq. (20) reflects the non-conservative nature of the BN equations. Therefore, different mechanisms of CWs propagation are inherent in the BN and KTGM models. It was supposed in (Houim and Oran, 2016) that the BN equations are poorly suited for describing waves in granular media and are better suited for describing mixtures with particles volume fraction close to packing limit. Now we have an opportunity to compare simulation results for the same problem obtained using the models that explicitly contain either Eq. (20) (author's simulations) or (21). Eq. (21) was explicitly included in the model (Kutushev and Rudakov, 1993) in which the same experiment (Gelfand et al., 1989) was considered. It should be noted that intergranular stresses model in (Kutushev and Rudakov, 1993) took into account nonlinear-elastic effects during loading-unloading of the particles.

In simulation (Kutushev and Rudakov, 1993), oscillations were obtained on the pressure curve on the wall under the layer (see Fig. 10). However, the first pressure peak was described less precisely quantitatively (the differences in the amplitude and the width reaches 50%) in comparison with the author's simulations. In addition, the pressure curve reached the level different from the experiment. The oscillations following the first pressure peak were described not quite right when compared to the experiment because the amplitude of the following peaks was only slightly less than of the first computed one. The explanation of the pressure oscillations was the following. Gas filtration provided constantly rising pressure under the layer. Separate "splashes" were determined by the compression and rarefaction of the solid skeleton of the layer. The plot of configuration pressure in (Kutushev and Rudakov, 1993) shows that the "splashes" corresponded to the moments when it was not zero on the wall. The term "splash" from (Kutushev and Rudakov, 1993) emphasized that qualitatively the character of secondary pulsations was similar to Fig. 14, not Fig. 15. Separate peaks were superimposed on the monotonically increasing curve, as it happened in Fig. 14. This is especially noticeable for the third peak, see the orange curve in Fig. 10. Thus, although we managed to obtain similar regime in our reversible BN simulations by means of variation of parameters in (2) – (6), commonly realized flow field from Fig. 9 do not give a premise for oscillations occurrence. In contrast, irreversible compaction model contains oscillations as its essential part according to the mechanism described in Section 5.3 but this mechanism is indeed different from that revealed in (Kutushev and Rudakov, 1993).

The essence of the experiment considered in (Gelfand et al., 1989) was later repeated in the work (Britan et al., 1997) already discussed in the Introduction. The authors in (Britan et al., 1997) used an improved experimental setup and investigated different mixtures of particles. These experiments were simulated in (Gubaidullin et al., 2003), where a two-speed model of a saturated porous medium with two stress tensors was used (Nugmatulin, 1990). In this model, there is no explicit expression for intergranular stresses with a switch upon reaching a certain volume fraction

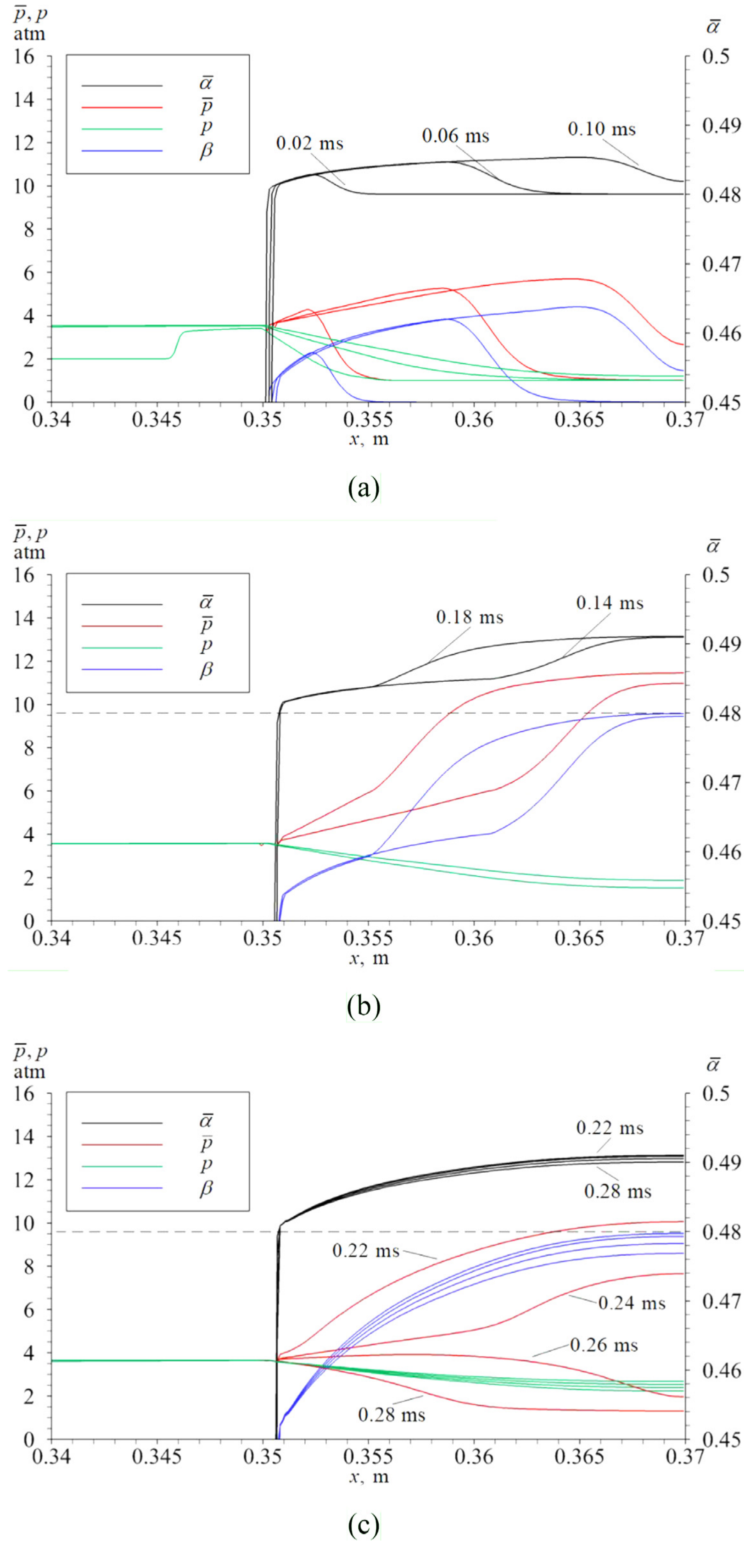

Fig. 16. Predicted spatial profiles of the solid phase volume fraction, solid phase pressure, gas phase pressure and configuration pressure at the successive time moments. Irreversible compaction case; $\bar{\alpha}_{\text{crit}} = 0.48$, $a = 10^5$ J/kg, $n = 1.02$.

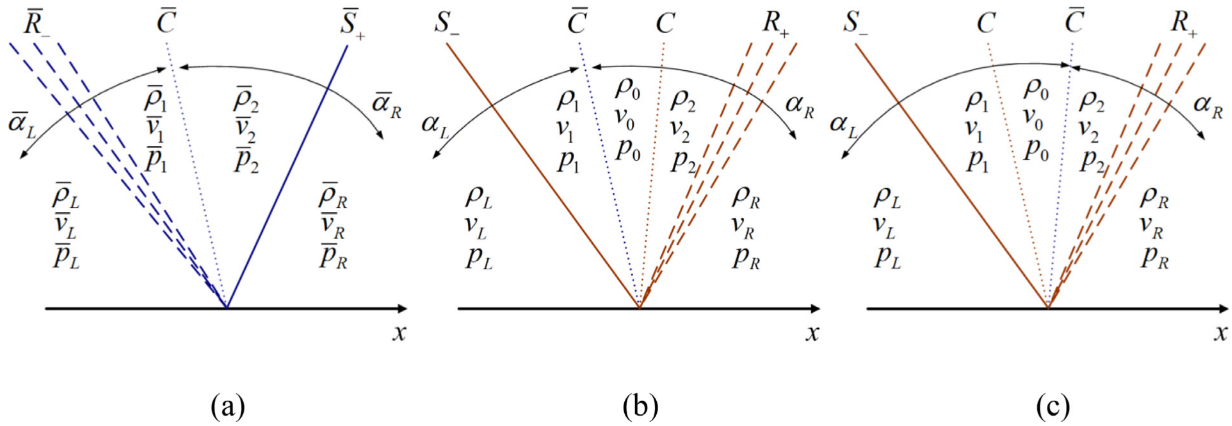

Fig. 17. The schematic of the Riemann problem solution of the BN system of equations in the subsonic case (Schwendeman et al., 2006). General case when both phases exist to the left and to the right from the discontinuity. All notations are standard, see (Toro, 2009).

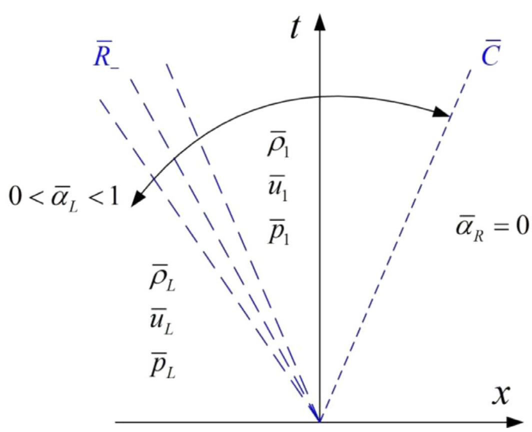

Fig. 18. The schematic of the Riemann problem solution of the BN system of equations in case of the absence of the solid phase to the right from the solid contact.

of particles. In simulations, the experimental statements were considered for the layers with the thicknesses from 10 mm to 40 mm, porosities from 0.389 to 0.456, particle diameters from 0.225 mm to 1.665 mm and incident SW Mach number about 1.32. In the majority of simulations, the predicted pressure curves did not demonstrate oscillations after the first peak although the correspondent experimental data did. At the same time there were several simulations with damping oscillations that qualitatively differed from oscillations in (Kutushev and Rudakov, 1993) and were similar to Fig. 15. These were not the additional solid pressure peaks superimposed on the gas pressure but sinusoidal pulsations. The necessity of taking into account plastic phenomena even at small cyclic loads was indicated as one of the factors affecting the difference between the predicted and experimental data in (Gubaidullin et al., 2003). So in fact the authors spoke in favor of using irreversible compaction model.

7. Conclusions

1. Thus, we continued our research (Utkin, 2019) on the features of the application of the Godunov method for the solution of the BN equations applied to practical problems in the field of two-phase granular media flows. This time we have developed a robust computational algorithm that allows solving problems with explicit interphase boundaries and accounting for the effects of intergranular stresses in the solid phase. The algorithm was based on the Godunov method (Schwendeman et al., 2006) – in a sense, the most general and accurate possible method for the Riemann problem solution. The algorithm also includes the pressure relaxation procedure which goes back to the works of R. Saurel and coauthors. Two approaches for the pressure relaxation were considered. The first one corresponds to the stiff local interfacial boundary equilibrium and so the reversible loading-unloading of the particles layer. The second approach implements irreversible compaction of the particles. The computational algorithm of the Godunov method was described in detail, including the analysis of all cases of the solid phase volume fraction ratio in adjacent computational cells. Computer C++ code (Computer Code for the Godunov Solver, 2020) is available that implements the Godunov solver for the BN equations in case of presence of a solid phase volume fraction gap in the neighbor cells. Pressure relaxation procedure taking into account intergranular stresses in the solid phase of particles was also descried in detail.
2. The developed algorithm was used to simulate an experiment (Gelfand et al., 1989) devoted to the normal incidence of a SW on a dense layer of particles near a rigid wall. As in many other studies the first peak on the pressure curve under the layer of particles was associated with the propagation of a CW through the layer and its subsequent reflection from the wall. A parametric study of the influence of parameters in the intergranular stresses model (Saurel et al., 2010) was carried out. The obtained set of parameters provided a difference of 15% in the value of the peak amplitude in the simulation and the experiment. However, the model of reversible loading-unloading of the layer did not provide oscillations of the pressure curve. On the contrary, irreversible compaction model contains such oscillations also observed in the experiment as an essential part.

Declaration of Competing Interest

No potential competing interest was reported by the authors.

CRediT authorship contribution statement

Ya.E. Poroshyna: Software, Validation, Formal analysis, Investigation, Writing – original draft. **P.S. Utkin:** Conceptualization, Methodology, Software, Validation, Writing – original draft, Writing – review & editing, Supervision.

Acknowledgments

This work was supported by the Russian Science Foundation, project no. 17-11-01293-P. The authors are grateful to the anonymous referees who helped to improve significantly the quality of the manuscript.

Appendix. Finding Gas and Solid Pressure at the Solid Contact

Both phases are present in the neighbor cells

Fig. 2a represents the case where two phases are present in the neighbor cells meaning that each of the parameters $\bar{\alpha}_i^{n+}$ and $\bar{\alpha}_{i+1}^{n-}$ are greater than $\varepsilon_{\text{disp\_abs}}$ in both cells i and $(i+1)$. For the states $\mathbf{U}_L$ and $\mathbf{U}_R$ from different sides of the discontinuity in this case the following system of equations is solved:

$$\mathbf{N}(p_1, p_2, \bar{p}_1, \bar{p}_2) = \mathbf{0}, \tag{22}$$

$$\begin{cases} N_1 = \overline{v}_2 - \overline{v}_1, \\ N_2 = \alpha_R\left(\frac{p_2+\pi_0}{p_1+\pi_0}\right)^{1/\gamma}\Delta v_2 - \alpha_L \Delta v_1, \\ N_3 = \overline{\alpha}_R\overline{p}_2 + \alpha_R p_2 - \overline{\alpha}_L\overline{p}_1 - \alpha_L p_1 + \alpha_L\rho_1\Delta v_1\Delta v, \\ N_4 = \frac{(p_2+\pi_0)\gamma}{(\gamma-1)\rho_1}\left(\frac{p_1+\pi_0}{p_2+\pi_0}\right)^{1/\gamma} + \frac{1}{2}\left(\Delta v_2^2 - \Delta v_1^2\right) - \frac{(p_1+\pi_0)\gamma}{(\gamma-1)\rho_1}, \end{cases} \text{if } v_1 > \overline{v}_1, \tag{23}$$

$$\begin{cases} N_1 = \overline{v}_2 - \overline{v}_1, \\ N_2 = \alpha_R \Delta v_2 - \alpha_L\left(\frac{p_1+\pi_0}{p_2+\pi_0}\right)^{1/\gamma}\Delta v_1, \\ N_3 = \overline{\alpha}_R\overline{p}_2 + \alpha_R p_2 - \overline{\alpha}_L\overline{p}_1 - \alpha_L p_1 + \alpha_R\rho_2\Delta v_2\Delta v, \\ N_4 = \frac{(p_2+\pi_0)\gamma}{(\gamma-1)\rho_2} + \frac{1}{2}\left(\Delta v_2^2 - \Delta v_1^2\right) - \frac{(p_1+\pi_0)\gamma}{(\gamma-1)\rho_2}\left(\frac{p_2+\pi_0}{p_1+\pi_0}\right)^{1/\gamma}, \end{cases} \text{if } v_1 < \overline{v}_1. \tag{24}$$

where $\Delta v_1 = v_1 - \overline{v}_1$, $\Delta v_2 = v_2 - \overline{v}_2$, $\Delta v = v_2 - v_1$. The system (23) corresponds to the configuration of waves described in Fig. 17b while the system (24) agrees with the Fig. 17c. The subscript "0" on Fig. 17b, c denotes the intermediate state between the solid and gas contacts. The subscripts 1 and 2 denote the states to the left and to the right of the solid contact.

The relations connected density and velocity with the pressure in gas phase:

$$v_1 = v_L - F_L(p_1),\ \rho_1 = G_L(p_1),\ v_2 = v_R + F_R(p_2),\ \rho_2 = G_R(p_2). \tag{25}$$

The analogous relations for the solid phase:

$$\overline{v}_1 = \overline{v}_L - \overline{F}_L(\overline{p}_1),\ \overline{\rho}_1 = \overline{G}_L(\overline{p}_1),\ \overline{v}_2 = \overline{v}_R + \overline{F}_R(\overline{p}_2),\ \overline{\rho}_2 = \overline{G}_R(\overline{p}_2), \tag{26}$$

where:

$$F_S(p) = \begin{cases} (p - p_s)\left[\frac{A_s}{p+\pi_0+B_s}\right]^{1/2}, \text{ if } p > p_s \text{ (shock wave)}, \\ \frac{2a_s}{(\gamma-1)}\left[\left(\frac{p+\pi_0}{p_s+\pi_0}\right)^{(\gamma-1)/2\gamma} - 1\right], \text{ if } p < p_s \text{ (rarefaction wave)}, \end{cases}$$

$$G_S(p) = \begin{cases} \rho_s\left[\frac{(\gamma-1)(p_s+\pi_0)+(\gamma+1)(p+\pi_0)}{(\gamma-1)(p+\pi_0)+(\gamma+1)(p_s+\pi_0)}\right], \text{ if } p > p_s \text{ (shock wave)}, \\ \rho_s\left(\frac{p+\pi_0}{p_s+\pi_0}\right)^{1/\gamma}, \text{ if } p < p_s \text{ (rarefaction wave)}, \end{cases}$$

with:

$A_s = \frac{2}{(\gamma+1)\rho_s}$, $B_s = \frac{(\gamma-1)}{(\gamma+1)}(p_s + \pi_0)$, $a_s = \sqrt{\frac{\gamma(p_s+\pi_0)}{\rho_s}}$, $s = L, R$.

The expressions $\bar{F}_S(\bar{p})$ and $\bar{G}_S(\bar{p})$ are the same as written above with adding upper bar for all variables.

The solution of the algebraic non-linear system of Eq. (22) using Newton method demands the construction of the Jacobian. Its components for the system (23) are:

$$\frac{\partial N_1}{\partial p_1} = 0,\ \frac{\partial N_1}{\partial p_2} = 0,\ \frac{\partial N_1}{\partial \overline{p}_1} = \frac{d\overline{F}_L}{d\overline{p}_1},\ \frac{\partial N_1}{\partial \overline{p}_2} = \frac{d\overline{F}_R}{d\overline{p}_2},$$

$$\frac{\partial N_2}{\partial p_1} = -\frac{\alpha_R}{\gamma(p_1+\pi_0)}\left(\frac{p_2+\pi_0}{p_1+\pi_0}\right)^{1/\gamma}\Delta v_2 + \alpha_L\frac{dF_L}{dp_1},$$

$$\frac{\partial N_2}{\partial p_2} = \alpha_R\left(\frac{p_2+\pi_0}{p_1+\pi_0}\right)^{1/\gamma}\left(\frac{\Delta v_2}{\gamma(p_2+\pi_0)} + \frac{dF_R}{dp_2}\right),\ \frac{\partial N_2}{\partial \overline{p}_1} = -\alpha_L\frac{d\overline{F}_L}{d\overline{p}_1},\ \frac{\partial N_2}{\partial \overline{p}_2} = -\alpha_R\left(\frac{p_2+\pi_0}{p_1+\pi_0}\right)^{1/\gamma}\frac{d\overline{F}_R}{d\overline{p}_2},$$

$$\frac{\partial N_3}{\partial p_1} = -\alpha_L + \alpha_L\frac{dG_L}{dp_1}\Delta v_1\Delta v + \alpha_L\rho_1(\Delta v_1 - \Delta v)\frac{dF_L}{dp_1},$$

$$\frac{\partial N_3}{\partial p_2} = \alpha_R + \alpha_L\rho_1\Delta v_1\frac{dF_R}{dp_2},\ \frac{\partial N_3}{\partial \overline{p}_1} = -\overline{\alpha}_L + \alpha_L\rho_1\Delta v\frac{d\overline{F}_L}{d\overline{p}_1},\ \frac{\partial N_3}{\partial \overline{p}_2} = \overline{\alpha}_R,$$

$$\frac{\partial N_4}{\partial p_1} = \frac{(p_2+\pi_0)}{(\gamma-1)\rho_1}\left(\frac{p_1+\pi_0}{p_2+\pi_0}\right)^{1/\gamma}\left(\frac{1}{(p_1+\pi_0)} - \frac{\gamma}{\rho_1}\frac{dG_L}{dp_1}\right) + \frac{\gamma}{(\gamma-1)\rho_1}\left(\frac{p_1}{\rho_1}\frac{dG_L}{dp_1} - 1\right) + \Delta v_1\frac{dF_L}{dp_1},$$

$$\frac{\partial N_4}{\partial p_2} = \frac{1}{\rho_1}\left(\frac{p_1+\pi_0}{p_2+\pi_0}\right)^{1/\gamma} + \Delta v_2\frac{dF_R}{dp_2},\ \frac{\partial N_4}{\partial \overline{p}_1} = -\Delta v_1\frac{d\overline{F}_L}{d\overline{p}_1},\ \frac{\partial N_4}{\partial \overline{p}_2} = -\Delta v_2\frac{d\overline{F}_R}{d\overline{p}_2}.$$

The Jacobian components for the system (24) are the following:

$$\frac{\partial N_1}{\partial p_1}=0,\ \frac{\partial N_1}{\partial p_2}=0,\ \frac{\partial N_1}{\partial \overline{p}_1}=\frac{d\overline{F}_L}{d\overline{p}_1},\ \frac{\partial N_1}{\partial \overline{p}_2}=\frac{d\overline{F}_R}{d\overline{p}_2},$$

$$\frac{\partial N_2}{\partial p_1}=\alpha_L\left(\frac{p_1+\pi_0}{p_2+\pi_0}\right)^{1/\gamma}\left(\frac{dF_L}{dp_1}-\frac{1}{\gamma(p_1+\pi_0)}\right),\ \frac{\partial N_2}{\partial p_2}=\frac{\alpha_L}{\gamma(p_2+\pi_0)}\left(\frac{p_1+\pi_0}{p_2+\pi_0}\right)^{1/\gamma}\Delta v_1+\alpha_R\frac{dF_R}{dp_2},\ \frac{\partial N_2}{\partial \overline{p}_1}=-\alpha_L\left(\frac{p_1+\pi_0}{p_2+\pi_0}\right)^{1/\gamma}\frac{d\overline{F}_L}{d\overline{p}_1},\ \frac{\partial N_2}{\partial \overline{p}_2}=-\alpha_R\frac{d\overline{F}_R}{d\overline{p}_2},$$

$$\frac{\partial N_3}{\partial p_1}=-\alpha_L+\alpha_R\rho_2\Delta v_2\frac{dF_L}{dp_1},\ \frac{\partial N_3}{\partial p_2}=\alpha_R+\alpha_R\Delta v_2\Delta v\frac{dG_R}{dp_2}+\alpha_R\rho_2(\Delta v+\Delta v_2)\frac{dF_R}{dp_2},$$

$$\frac{\partial N_3}{\partial \overline{p}_1}=-\overline{\alpha}_L,\ \frac{\partial N_3}{\partial \overline{p}_2}=\overline{\alpha}_R-\alpha_R\rho_2\Delta v\frac{dF_R}{d\overline{p}_2},$$

$$\frac{\partial N_4}{\partial p_1}=-\frac{1}{\rho_2}\left(\frac{p_2+\pi_0}{p_1+\pi_0}\right)^{1/\gamma}+\Delta v_1\frac{dF_L}{dp_1},$$

$$\frac{\partial N_4}{\partial p_2}=\frac{\gamma}{(\gamma-1)\rho_2}+\frac{\gamma}{(\gamma-1)\rho_2^2}\frac{\partial G_R}{\partial p_2}\left[(p_1+\pi_0)\left(\frac{p_2+\pi_0}{p_1+\pi_0}\right)^{1/\gamma}-(p_2+\pi_0)\right]+ \\ +\Delta v_2\frac{\partial F_R}{\partial p_2}-\frac{(p_1+\pi_0)}{(\gamma-1)(p_2+\pi_0)\rho_2}\left(\frac{p_2+\pi_0}{p_1+\pi_0}\right)^{1/\gamma},$$

$$\frac{\partial N_4}{\partial \overline{p}_1}=-\Delta v_1\frac{d\overline{F}_L}{d\overline{p}_1},\ \frac{\partial N_4}{\partial \overline{p}_2}=-\Delta v_2\frac{d\overline{F}_R}{d\overline{p}_2}.$$

This case was realized in (Computer Code for the Godunov Solver, 2020).

The solid phase is present only to the left from the solid contact

Figs. 2b and 18 represent the case when $\bar{\alpha}$ is very small to the right from the solid contact. In this special case the following system of equations is solved:

$$\tilde{\mathbf{N}}(p_1,p_2,\bar{p}_1)=\mathbf{0},$$

$$\begin{cases} \tilde{N}_1=\left(\frac{p_2+\pi_0}{p_1+\pi_0}\right)^{1/\gamma}\delta v_L-\alpha_L\Delta v_1, \\ \tilde{N}_2=p_2-\overline{\alpha}_L\overline{p}_1-\alpha_L p_1+\alpha_L\rho_1\Delta v_1\Delta v, & \text{if } v_1>\overline{v}_1, \\ \tilde{N}_3=\frac{(p_2+\pi_0)\gamma}{(\gamma-1)\rho_1}\left(\frac{p_1+\pi_0}{p_2+\pi_0}\right)^{1/\gamma}+\frac{1}{2}\left(\delta {v_L}^2-\Delta v_1^2\right)-\frac{(p_1+\pi_0)\gamma}{(\gamma-1)\rho_1}, \end{cases} \tag{27}$$

$$\begin{cases} \tilde{N}_1=\delta v_L-\alpha_L\left(\frac{p_1+\pi_0}{p_2+\pi_0}\right)^{1/\gamma}\Delta v_1, \\ \tilde{N}_2=p_2-\overline{\alpha}_L\overline{p}_1-\alpha_L p_1+\alpha_R\rho_2\Delta v_2\Delta v, & \text{if } v_1<\overline{v}_1, \\ \tilde{N}_3=\frac{(p_2+\pi_0)\gamma}{(\gamma-1)\rho_2}+\frac{1}{2}\left(\delta {v_L}^2-\Delta v_1^2\right)-\frac{(p_1+\pi_0)\gamma}{(\gamma-1)\rho_2}\left(\frac{p_2+\pi_0}{p_1+\pi_0}\right)^{1/\gamma}, \end{cases} \tag{28}$$

where $\delta v_L=v_2-\bar{v}_1$. These systems of equations are obtained from (23) and (24) with the help of formal substitution $\bar{\alpha}_L\to 0$ and $\bar{v}_1\to\bar{v}_2$. The Jacobian components for the system (27) are the following:

$$\frac{\partial \tilde{N}_1}{\partial p_1}=-\left(\frac{p_2+\pi_0}{p_1+\pi_0}\right)^{1/\gamma}\frac{\delta v_L}{\gamma(p_1+\pi_0)}+\alpha_L\frac{dF_L}{dp_1},\ \frac{\partial \tilde{N}_1}{\partial p_2}=\left(\frac{p_2+\pi_0}{p_1+\pi_0}\right)^{1/\gamma}\frac{\delta v_L}{\gamma(p_2+\pi_0)}+\left(\frac{p_2+\pi_0}{p_1+\pi_0}\right)^{1/\gamma}\frac{dF_R}{dp_2},$$

$$\frac{\partial \tilde{N}_1}{\partial \bar{p}_1}=\left(\frac{p_2+\pi_0}{p_1+\pi_0}\right)^{1/\gamma}\frac{d\bar{F}_L}{d\bar{p}_1}-\alpha_L\frac{d\bar{F}_L}{d\bar{p}_1},$$

$$\frac{\partial \tilde{N}_2}{\partial p_1}=\frac{dF_L}{dp_1}\alpha_L\rho_1(\Delta v_1-\Delta v)+\alpha_L\left(\frac{dG_L}{dp_1}\Delta v_1\Delta v-1\right),\ \frac{\partial \tilde{N}_2}{\partial p_2}=1+\alpha_L\rho_1\Delta v_1\frac{dF_R}{dp_2},$$

$$\frac{\partial \tilde{N}_2}{\partial \bar{p}_1}=-\bar{\alpha}_L+\alpha_L\rho_1\Delta v_1\frac{d\bar{F}_L}{d\bar{p}_1},$$

$$\frac{\partial \tilde{N}_3}{\partial p_1}=\frac{\gamma}{(\gamma-1)\rho_1}\left(\frac{p_1+\pi_0}{p_2+\pi_0}\right)^{1/\gamma-1}-\left(\frac{p_1+\pi_0}{p_2+\pi_0}\right)^{1/\gamma}\frac{\gamma(p_2+\pi_0)}{(\gamma-1)\rho_1^2}\frac{dG_L}{dp_1}+ \\ +\frac{(p_1+\pi_0)\gamma}{(\gamma-1)\rho_1^2}\frac{dG_L}{dp_1}-\frac{\gamma}{(\gamma-1)\rho_1}+\Delta v_1\frac{dF_L}{dp_1},$$

$$\frac{\partial \tilde{N}_3}{\partial p_2}=\frac{1}{\rho_1}\left(\frac{p_1+\pi_0}{p_2+\pi_0}\right)^{1/\gamma}+\delta v_L\frac{dF_R}{dp_2},\ \frac{\partial \tilde{N}_3}{\partial \overline{p}_1}=\Delta v\frac{d\overline{F}_L}{d\overline{p}_1}.$$

The Jacobian components for the system (28) are the following:

$$\frac{\partial \tilde{N}_1}{\partial p_1}=\alpha_L\left(\frac{p_1+\pi_0}{p_2+\pi_0}\right)^{1/\gamma}\left(\frac{dF_L}{dp_1}-\frac{\Delta v_1}{\gamma(p_1+\pi_0)}\right),\ \frac{\partial \tilde{N}_1}{\partial p_2}=\frac{dF_R}{dp_2}+\alpha_L\left(\frac{p_1+\pi_0}{p_2+\pi_0}\right)^{1/\gamma}\frac{\Delta v_1}{\gamma(p_2+\pi_0)},$$

$$\frac{\partial \tilde{N}_1}{\partial \bar{p}_1} = \frac{d\bar{F}_L}{d\bar{p}_1}\left(1 - \alpha_L\left(\frac{p_1+\pi_0}{p_2+\pi_0}\right)^{1/\gamma}\right),$$

$$\frac{\partial \tilde{N}_2}{\partial p_1} = -\alpha_L + \rho_2\frac{dF_L}{dp_1}\delta\upsilon_L,\ \frac{\partial \tilde{N}_2}{\partial p_2} = 1 + \frac{dG_R}{dp_2}\delta\upsilon_L\Delta\upsilon + \rho_2\frac{dF_R}{dp_2}(\Delta\upsilon + \delta\upsilon_L),\ \frac{\partial \tilde{N}_2}{\partial \overline{p}_1} = -\overline{\alpha}_L + \rho_2\frac{d\overline{F}_L}{d\overline{p}_1}\Delta\upsilon,$$

$$\frac{\partial \tilde{N}_3}{\partial p_1} = -\frac{1}{\rho_1}\left(\frac{p_2+\pi_0}{p_1+\pi_0}\right)^{1/\gamma} + \Delta\upsilon_1\frac{dF_L}{dp_1},$$

$$\frac{\partial \tilde{N}_3}{\partial p_2} = \frac{\gamma}{(\gamma-1)\rho_2} - \frac{(p_2+\pi_0)\gamma}{(\gamma-1)\rho_2^2}\frac{dG_R}{dp_2} + \delta\upsilon_L\frac{dF_R}{dp_2} - \left(\frac{p_2+\pi_0}{p_1+\pi_0}\right)^{1/\gamma-1}\frac{1}{(\gamma-1)\rho_2}\frac{dG_R}{dp_2},\ \frac{\partial \tilde{N}_3}{\partial \overline{p}_1} = \Delta\upsilon\frac{d\overline{F}_L}{d\overline{p}_1}.$$

The solid phase is present only to the right from the solid contact

The system of equations for the special case of absence of the solid phase to the left from the solid contact is the following: $\tilde{\mathbf{N}}(p_1, p_2, \bar{p}_2) = \mathbf{0}$,

$$\begin{cases} \tilde{N}_1 = \alpha_R\left(\frac{p_2+\pi_0}{p_1+\pi_0}\right)^{1/\gamma}\Delta\upsilon_2 - \delta\upsilon_R, \\ \tilde{N}_2 = \overline{\alpha}_R\overline{p}_2 + \alpha_R p_2 - p_1 + \rho_1\delta\upsilon_R\Delta\upsilon, \\ \tilde{N}_3 = \frac{\gamma(p_1+\pi_0)}{(\gamma-1)\rho_1}\left(\left(\frac{p_1+\pi_0}{p_2+\pi_0}\right)^{1/\gamma-1} - 1\right) + \frac{1}{2}\left(\Delta\upsilon_2{}^2 - \delta\upsilon_R{}^2\right), \end{cases} \quad \text{if } \upsilon_1 > \overline{\upsilon}_1, \tag{29}$$

$$\begin{cases} \tilde{N}_1 = \alpha_R\Delta\upsilon_2 - \delta\upsilon_R\left(\frac{p_1+\pi_0}{p_2+\pi_0}\right)^{1/\gamma}, \\ \tilde{N}_2 = \overline{\alpha}_R\overline{p}_2 + \alpha_R p_2 - p_1 + \alpha_R\rho_2\Delta\upsilon_2\Delta\upsilon, \\ \tilde{N}_3 = \frac{\gamma(p_2+\pi_0)}{(\gamma-1)\rho_2}\left(1 - \left(\frac{p_2+\pi_0}{p_1+\pi_0}\right)^{1/\gamma-1}\right) + \frac{1}{2}\left(\Delta\upsilon_2^2 - \delta\upsilon_R^2\right), \end{cases} \quad \text{if } \upsilon_1 < \overline{\upsilon}_1, \tag{30}$$

where $\delta\upsilon_R = \upsilon_1 - \bar{\upsilon}_2$. The Jacobian components for the system (29) are the following:

$$\frac{\partial \tilde{N}_1}{\partial p_1} = -\alpha_R\left(\frac{p_2+\pi_0}{p_1+\pi_0}\right)^{1/\gamma}\frac{\Delta\upsilon_2}{\gamma(p_1+\pi_0)} + \frac{dF_L}{dp_1},\ \frac{\partial \tilde{N}_1}{\partial p_2} = \alpha_R\left(\frac{p_2+\pi_0}{p_1+\pi_0}\right)^{1/\gamma}\left(\frac{\Delta\upsilon_2}{\gamma(p_2+\pi_0)} + \frac{dF_R}{dp_2}\right),$$

$$\frac{\partial \tilde{N}_1}{\partial \bar{p}_2} = \left(1 - \alpha_R\left(\frac{p_2+\pi_0}{p_1+\pi_0}\right)^{1/\gamma}\right)\frac{d\bar{F}_R}{d\bar{p}_2},$$

$$\frac{\partial \tilde{N}_2}{\partial p_1} = -1 + \rho_1\delta\upsilon_R\frac{dF_L}{dp_1}(\delta\upsilon_R - \Delta\upsilon) + \delta\upsilon_R\Delta\upsilon\frac{dG_L}{dp_1},\ \frac{\partial \tilde{N}_2}{\partial p_2} = \alpha_R + \rho_1\delta\upsilon_R\frac{dF_R}{dp_2},\ \frac{\partial \tilde{N}_2}{\partial \overline{p}_2} = \overline{\alpha}_R - \rho_1\Delta\upsilon\frac{d\overline{F}_R}{d\overline{p}_2},$$

$$\frac{\partial \tilde{N}_3}{\partial p_1} = \frac{1}{(\gamma-1)\rho_1}\left(\left(\frac{p_1+\pi_0}{p_2+\pi_0}\right)^{1/\gamma-1} - \gamma\right) + \frac{\gamma(p_1+\pi_0)}{(\gamma-1)\rho_1^2}\frac{dG_L}{dp_1}\left(1 - \left(\frac{p_1+\pi_0}{p_2+\pi_0}\right)^{1/\gamma-1}\right) + \delta\upsilon_R\frac{dF_L}{dp_1},$$

$$\frac{\partial \tilde{N}_3}{\partial p_2} = \frac{1}{\rho_1}\left(\frac{p_1+\pi_0}{p_2+\pi_0}\right)^{1/\gamma} + \delta\upsilon_R\frac{dF_R}{dp_2},\ \frac{\partial \tilde{N}_3}{\partial \overline{p}_2} = -\Delta\upsilon\frac{d\overline{F}_R}{d\overline{p}_2}.$$

The Jacobian components for the system (30) are the following:

$$\frac{\partial \tilde{N}_1}{\partial p_1} = \left(\frac{p_1+\pi_0}{p_2+\pi_0}\right)^{1/\gamma}\left(\frac{dF_L}{dp_1} - \frac{\delta\upsilon_R}{\gamma(p_1+\pi_0)}\right),\ \frac{\partial \tilde{N}_1}{\partial p_2} = \left(\frac{p_1+\pi_0}{p_2+\pi_0}\right)^{1/\gamma}\frac{\Delta\upsilon_2}{\gamma(p_2+\pi_0)} + \alpha_R\frac{dF_R}{dp_2},$$

$$\frac{\partial \tilde{N}_1}{\partial \bar{p}_2} = \left(\left(\frac{p_1+\pi_0}{p_2+\pi_0}\right)^{1/\gamma} - \alpha_R\right)\frac{d\bar{F}_R}{d\bar{p}_2},$$

$$\frac{\partial \tilde{N}_2}{\partial p_1} = -1 + \alpha_R\rho_2\Delta\upsilon_2\frac{dF_L}{dp_1},\ \frac{\partial \tilde{N}_2}{\partial p_2} = \alpha_R\left(1 + \frac{dG_R}{dp_2}\Delta\upsilon_2\Delta\upsilon + \rho_2\frac{dF_R}{dp_2}(\Delta\upsilon + \Delta\upsilon_2)\right),$$

$$\frac{\partial \tilde{N}_2}{\partial \bar{p}_2} = \bar{\alpha}_R - \alpha_R\rho_2\Delta\upsilon\frac{d\bar{F}_R}{d\bar{p}_2},$$

$$\frac{\partial \tilde{N}_3}{\partial p_1} = -\frac{1}{\rho_2}\left(\frac{p_2+\pi_0}{p_1+\pi_0}\right)^{1/\gamma} + \delta\upsilon_R\frac{dF_L}{dp_1},$$

$$\frac{\partial \tilde{N}_3}{\partial p_2} = \frac{\gamma}{(\gamma-1)\rho_2} + \frac{\gamma(p_2+\pi_0)}{(\gamma-1)\rho_2^2}\frac{\partial G_R}{\partial p_2}\left[\left(\frac{p_2+\pi_0}{p_1+\pi_0}\right)^{1/\gamma-1} - 1\right] - \frac{1}{(\gamma-1)\rho_2}\left(\frac{p_2+\pi_0}{p_1+\pi_0}\right)^{1/\gamma-1} + \Delta\upsilon_2\frac{dF_R}{dp_2},$$

$$\frac{\partial \tilde{N}_3}{\partial \bar{p}_2} = -\Delta\upsilon\frac{d\bar{F}_R}{d\bar{p}_2}.$$

References

Abgrall, R., Saurel, R., 2003. Discrete equations for physical and numerical compressible multiphase mixtures. J. Comp. Phys. 186, 361–396. doi:10.1016/S0021-9991(03)00011-1.

Baer, M.R., Nunziato, J.W., 1986. A two-phase mixture theory for the deflagration-to-detonation transition (DDT) in reactive granular materials. Int. J. Multiph. Flow 12, 861–889. doi:10.1016/0301-9322(86)90033-9.

Baer, M.R., 1988. Numerical studies of dynamic compaction of inert and energetic granular materials. Appl. Mech. 55, 36–43. doi:10.1115/1.3173658.

Baer, M.R., 1992. A numerical study of shock wave reflections on low density foam. Shock Waves 2, 121–124. doi:10.1007/BF01415901.

Bdzil, J.B., Menikoff, R., Son, S., Kapila, A.K., Stewart, D.S., 1999. Two-phase modelling of DDT in granular materials: a critical examination of modeling issues. Phys. Fluids 11, 378–402. doi:10.1063/1.869887.

Ben-Dor, G., Mazor, G., Igra, O., Sorek, S., Onodera, H., 1994. Shock wave interaction with cellular materials. Part II: open cell foams; experimental and numerical results. Shock Waves 3, 167–179. doi:10.1007/BF01414711.

Britan, A., Ben-Dor, G., Elperin, T., Igra, O., Jiang, J.P., 1997. Gas filtration during the impact of weak shock waves on granular layers. Int. J. Multiph. Flow 23, 473–491. doi:10.1016/S0301-9322(96)00088-2.

Britan, A., Ben-Dor, G., 2006. Shock tube study of the dynamical behavior of granular materials. Int. J. Multiph. Flow 32, 623–642. doi:10.1016/j.ijmultiphaseflow.2006.01.007.

Britan, A.B., Zinovik, I.N., Levin, V.A., Mitichkin, S.Yu., Testov, V.G., Haibo, H.u, 1995. Specific features of propagation of gas dynamic perturbations under the interaction between shock waves and two-phase media of foamy structure (in Russian). J. Tech. Phys. 65 (7), 19–28. https://journals.ioffe.ru/articles/viewPDF/19030.

Dumbser, M., Balsara, D.S., 2016. A new efficient formulation of the HLLEM Riemann solver for general conservative and non-conservative hyperbolic systems. J. Comp. Phys. 304, 275–319. doi:10.1016/j.jcp.2015.10.014.

Fan, B.C., Chen, Z.H., Jiang, X.H., Li, H.Z., 2007. Interaction of a shock wave with a loose dusty bulk layer. Shock Waves 16, 179–187. doi:10.1007/s00193-006-0059-5.

Favrie, N., Gavrilyuk, S., 2013. Dynamic compaction of granular materials. Proc. R. Soc. A. 469. doi:10.1098/rspa.2013.0214.

Fedorov, A.V., Fedorchenko, I.A., 2005. Computation of dust lifting behind a shock wave sliding along the layer. Verification of the Model. Comb., Expl. Shock Waves 41 (3), 336–345. doi:10.1007/s10573-005-0041-z.

Fraysse, F., Redondo, C., Rubio, G., Valero, E., 2016. Upwind methods for the Baer-Nunziato equations and higher-order reconstruction using artificial viscosity. J. Comp. Phys. 326, 805–827. doi:10.1016/j.jcp.2016.09.017.

Furfaro, D., Saurel, R., 2015. A simple HLLC-type Riemann solver for compressible non-equilibrium two-phase flows. Comp. Fluids 111, 159–178. doi:10.1016/j.compfluid.2015.01.016.

Gelfand, B.E., Gubin, S.A., Kogarko, S.M., Popov, O.E., 1975. Investigation of the special characteristics of propagation and reflection of pressure waves in a porous medium. J. Appl. Mech. Tech. Phys. 16, 897–900. doi:10.1007/BF00852818.

Gelfand, B.E., Medvedev, S.P., Borisov, A.A., Polenov, A.N., Frolov, S.M., Tsyganov, S.A., 1989. Shock loading of stratified dusty systems. Arch. Combust. 9 (4), 153–165. http://archcomb.itc.pw.edu.pl/volume-9-no-1-4-1989/shock-loading-of-stratified-dusty-systems-pp-153-166.

Gidaspow, D., 1994. Multiphase Flow and Fluidization. Academic Press.

Godunov, S.K., Zabrodin, A.V., Ya. Ivanov, M., Krayko, A.N., Prokopov, G.P., 1976. Numerical solution of multidimensional gas dynamics problems (in Russian). Nauka, Moscow,.

Gubaidullin, A.A., Britan, A., Dudko, D.N., 2003. Air shock wave interaction with an obstacle covered by porous material. Shock Waves 13, 41–48. doi:10.1007/s00193-003-0193-2.

Hennessey, M., Kapila, A.K., Schwendeman, D.W., 2020. An HLLC-type Riemann solver and high-resolution Godunov method for a two-phase model of reactive flow with general equations of state. J. Comp. Phys. 405, 109180. doi:10.1016/j.jcp.2019.109180.

Houim, R.W., Oran, E.S., 2016. A multiphase model for compressible granular-gaseous flows: formulation and initial tests. J. Fluid Mech. 789, 166–220. doi:10.1017/jfm.2015.728.

Khishchenko, K.V., Lomonosov, I.V., Fortov, V.E., 1996. Equations of state for organic compounds over wide range of densities and pressures. AIP Conf. Proc. 370, 125–128. doi:10.1063/1.50728.

Koo, K.K., Kuo, J.H., Davis, T.R., Coates, G.R., 1976. Transient combustion in mobile gas-permeable propellants. Acta Astronautica 3. doi:10.1016/0094-5765(76)90163-6, 573–559.

Kutushev, A.G., Rudakov, D.A., 1993. Numerical study of the action of a shock wave on an obstacle screened by a layer of porous powder material. J. Appl. Mech. Tech. Phys. 34 (5), 618–624. doi:10.1007/BF00859825.

Kutushev, A.G., Rodionov, S.P., 1999. Numerical study of the effect of the parameters of a bulk layer and an incident shock wave on the pressure at a shielded flat wall. Combust. Expl. Shock Waves 35 (2), 206–213. doi:10.1007/BF02674440.

Lallemand, M.-H., Chinnayya, A., Le Metayer, O., 2005. Pressure relaxation procedures for multiphase compressible flows. Int. J. Num. Meth. Fluids 49 (1), 1–56. doi:10.1002/fld.967.

Lochon, H., Daude, F., Galon, P., Herard, J.-M., 2016. HLLC-type Riemann solver with approximated two-phase contact for the computation of the Baer-Nunziato two-fluid model. J. Comp. Phys. 325, 733–762. doi:10.1016/j.jcp.2016.09.015.

Lide, D.R. (Ed.), 2005. Handbook of Chemistry and Physics, 85th Edition. CRC Press.

Mazor, G., Ben-Dor, G., Igra, O., Sorek, S., 1994. Shock waves interaction with cellular materials. Part I: analytical investigation and governing equations. Shock Waves 3, 159–165. doi:10.1007/BF01414710.

McGrath II, T.P., Clair, J.G.St., Balachandar, S., 2016. A compressible two-phase model for dispersed particle flows with application from dense to dilute regimes. J. Appl. Phys. 119, 174903. doi:10.1063/1.4948301.

Menshov, I., Serezhkin, A., 2018. A generalized Rusanov method for the Baer-Nunziato equations with application to DDT processes in condensed porous explosives. Int. J. Num. Meth. Fluids 86, 346–364. doi:10.1002/fld.4419.

Nigmatulin, R.I., 1990. Dynamics of Multiphase Media., 1, First edition CRC Press Volume.

Olim, M., van Dongen, M.E.H., Kitamura, T., Takayama, K., 1994. Numerical simulation of the propagation of shock waves in compressible open-cell porous foams. Int. J. Multiph. Flow 20 (3), 557–568. doi:10.1016/0301-9322(94)90029-9.

Rogue, X., Rodriguez, G., Haas, J.F., Saurel, R., 1998. Experimental and numerical investigation of the shock-induced fluidization of a particles bed. Shock Waves 8, 29–45. doi:10.1007/s001930050096.

Saurel, R., Abgrall, R., 1999. A multiphase Godunov method for compressible multifluid and multiphase flows. J. Comp. Phys. 150, 425–467. doi:10.1006/jcph.1999.6187.

Saurel, R., Lemetayer, O., 2001. A multiphase model for compressible flows with interfaces, shocks, detonation waves and cavitation. J. Fluid Mech. 431, 239–271. doi:10.1017/S0022112000003098.

Saurel, R., Favrie, N., Petitpas, F., Lallemand, M.-H., Gavrilyuk, S.L., 2010. Modelling dynamic and irreversible powder compaction. J. Fluid Mech. 664, 348–396. doi:10.1017/S0022112010003794.

Saurel, R., Matelot, S.Le L., Tosello, R., Lapébie, E., 2014. Symmetric model of compressible granular mixtures with permeable interfaces. Phys. Fluids. 26, 123304. doi:10.1063/1.4903259.

Saurel, R., Chinnayya, A., Carmouze, Q., 2017. Modelling compressible dense and dilute two-phase flows. Phys. Fluids 29, 063301. doi:10.1063/1.4985289.

Schwendeman, D.W., Wahle, C.W., Kapila, A.K., 2006. The Riemann problem and a high-resolution Godunov method for a model of compressible two-phase flow. J. Comp. Phys. 212, 490–526. doi:10.1016/j.jcp.2005.07.012.

Schwendeman, D.W., Wahle, C.W., Kapila, A.K., 2008. A study of detonation evolution and structure for a model of compressible two-phase reactive flow. Comb. Theory Modell. 12 (1), 159–204. doi:10.1080/13647830701564538.

Seitz, M.W., Skews, B.W., 2006. Effect of compressible foam properties on pressure amplification during shock wave impact. Shock Waves 15, 177–197. doi:10.1007/s00193-006-0033-2.

Skews, B.W., 1991. The reflected pressure field in the interaction of weak shock waves with a compressible foam. Shock Waves 1, 205–211. doi:10.1007/BF01413795.

Skews, B.W., Atkins, M.D., Seitz, M.W., 1993. The impact of a shock wave on porous compressible foams. J. Fluid Mech. 253, 245–265. doi:10.1017/S0022112093001788.

Sugiyama, Y., Homae, T., Matsumura, T., Wakabayashi, K., 2021. Numerical study on the mitigation effect of glass particles filling a partially confined space on a blast wave. Int. J. Multiph. Flow 136, 103546. doi:10.1016/j.ijmultiphaseflow.2020.103546.

Surov, V.S., 2000. Reflection of an air shock wave from a foam layer. High Temperature 38 (1), 97–105. doi:10.1007/BF02755574.

Tokareva, S.A., Toro, E.F., 2010. HLLC-type Riemann solver for the Baer-Nunziato equations of compressible two-phase flow. J. Comp. Phys. 229, 3573–3604. doi:10.1016/j.jcp.2010.01.016.

Tokareva, S.A., Toro, E.F., 2016. A flux splitting method for the Baer-Nunziato equations of compressible two-phase flow. J. Comp. Phys. 323, 45–74. doi:10.1016/j.jcp.2016.07.019.

Toro, E.F., 2009. Riemann Solvers and Numerical Methods for Fluid Dynamics, Third Edition Springer.

Utkin, P.S., 2017. Mathematical modeling of the interaction of a shock wave with a dense cloud of particles within the framework of the two-fluid approach. Russ. J. Phys. Chem. B. 11, 963–973. doi:10.1134/S1990793117050141.

Utkin, P.S., Fortova, S.V., 2018. Mathematical modeling of high-speed interaction of metallic plates within the two-fluid Euler approach. Comp. Math. Math. Phys. 58, 1377–1383. doi:10.1134/S0965542518080171.

Utkin, P.S., 2019. Numerical simulation of shock wave – dense particles cloud interaction using Godunov solver for Baer–Nunziato equations. Int. J. Num. Meth. Heat Fluid Flow 29 (9), 3225–3241. doi:10.1108/HFF-10-2018-0587.

Yasuhara, M., Watanabe, S., Kitagawa, K., Yasue, T., Mizutani, M., 1996. Experiment on effects of porosity in the interaction of shock wave and foam. JSME Int. J. B 39 (2), 287–293. doi:10.1299/jsmeb.39.287.

, 2020. Computer Code for the Godunov Solver for the Baer-Nunziato Equations. P.S. Utkin's Personal Web-Site http://fastproclab.16mb.com/Materials-for-papers/.